Thermal Science and Engineering Progress 65 (2025) 103856

Contents lists available at ScienceDirect

Thermal Science and Engineering Progress

journal homepage: www.elsevier.com/locate/tsep

Techno-economic and environmental assessment of a solar-powered multi-generation system for a sustainable energy, hydrogen and fresh-water production

Mattia De Rosa [a,b,*], Mehdi Aliehyaei [a,c]

[a] Department of Mechanical, Energy, Management and Transportation Engineering (DIME), University of Genoa, Via All'Opera Pia 15/A, 16145, Genova, Italy
[b] International Centre of Energy Resource Management (iCERM), Genoa Division, Italy
[c] Pardis Branch, Islamic Azad University, Pardis New City, Iran

ARTICLE INFO

Keywords:
Organic rankine cycles
Solar energy
Hydrogen
Fresh water production

ABSTRACT

This study presents a comprehensive 4E (energy, exergy, economic, and exergo-environmental) analysis of a solar-powered multi-generation system (MGS) that integrates parabolic trough collectors (PTCs), thermal energy storage (TES), an organic Rankine cycle (ORC), an absorption refrigeration cycle (ARC), a proton exchange membrane electrolyzer (PEME), and a reverse osmosis (RO) unit to simultaneously produce electricity, cooling, potable water, and hydrogen. A complete thermodynamic model is developed in Engineering Equation Solver (EES) to evaluate the system from technical, economic, and environmental perspectives.

Results indicate that the MGS can convert solar energy into multiple outputs with energy and exergy efficiencies of 12.2% and 4.3%, respectively. The highest and lowest energy efficiencies are found in PEME (58.6%) and ORC (7.4%), while the highest and lowest exergy efficiencies are related to PEME (57.4%) and PTC (11.9%), respectively. Despite notable environmental impacts from the complex subsystems (particularly PTC and PEME), the system demonstrates strong economic performance with a net present value of approximately USD 8 million, an internal rate of return of 30%, and a payback period of 3.8 years. Sensitivity analysis shows that increasing solar radiation reduces the number of required PTCs and shortens payback time, with less effect on energy and exergy efficiencies due to increased thermal and radiative losses.

1. Introduction

The depletion of fossil fuel resources and the growing concerns related to environmental pollution and global warming have drawn significant attention from governments and investors towards renewable energy. Solar energy has received special attention among these energy sources due to its wide range of applications and substantial potential. The heat harnessed from solar energy can be utilized for a wide range of applications, including direct heating and electricity generation. Solar energy systems can be designed to supply either a single useful energy output (e.g., heat, electricity, or cooling) or as multi-generation systems (MGS), which is capable of producing multiple outputs thereby enhancing system productivity and optimizing solar resource utilization [1–4].

Generally, solar-powered MGS utilizes solar radiation as the main energy source using solar collectors such as parabolic trough collectors (PTC), which converts it into heat, which can then be used for different purposes such as electricity generation, heat, cooling, or other indirect applications like potable water or hydrogen production.[5–7] Due to solar energy utilization, S-MGS systems can contribute to the reduction of carbon emissions, and they are a suitable choice particularly for regions with high availability of solar resources, providing a reliable and sustainable solution both for isolated areas with limited energy infrastructure available, and in urban settings. [8,9]. Furthermore, S-MGS may provide operational flexibility and meet diverse needs which can be tailored on local specific demands, despite higher capital investment related to greater layout complexity and an increase of land usage, which need to be correctly assessed and evaluated from a techno-economic and environmental point of view.[5–7].

Over the last years, extensive research has been conducted on S-MGS-powered solar energy that uses various types of solar collectors, typically based on parabolic solar collectors (PTC), to generate several product streams, based on the subsystems integrated into the MGS layout. These products or useful outputs may differ based on the geographic location, specific user needs, market, and economic contexts,

* Corresponding author at: Department of Mechanical, Energy, Management and Transportation Engineering (DIME), University of Genoa, Via All'Opera Pia 15/A, 16145, Genova, Italy.
E-mail addresses: mattia.derosa@unige.it (M. De Rosa), mehdi.aliehyaie@edu.unige.it (M. Aliehyaei).

https://doi.org/10.1016/j.tsep.2025.103856
Received 1 March 2025; Received in revised form 4 June 2025; Accepted 8 July 2025
Available online 25 July 2025

financial interests of investors, and local social aspects. Generally, from a technical point of view, adding subsystems to generate more useful outputs can increase the overall utilization ratio of the MSG [10], while economic and environmental aspects need to be carefully assessed based on each specific application.

One of the important products which may be produced in solar-powered S-MGS systems is represented by hydrogen, which is considered a promising next-generation fuel to substitute natural gas and used also as energy storage fuel [11]. For instance, Zheng et al. [12] investigated the hydrogen produced by proton exchange membrane electrolyzer (PEME) and used to store fuel for cooling and heating purposes. The addition of this system increased the overall energy and exergy efficiency by 80.7% and 33.8%, respectively. Moreover, the economic assessment of the proposed system showed a net present value (NPV) of USD 45.8M with a levelized cost of electricity (LCOE) of 0.0540 US$/kWh, and a payback period (PP) of 9.1 years.

Notwithstanding, one of the main limitations of solar-powered MSG is represented by its availability, which is limited to a certain number of hours, based on location, season, and hour of the day. Thus, extending the operating hours of solar-based systems requires the installation of thermal energy storage (TES), which represents a common sub-system integrated into S-MSG systems, especially for large installations. Typically, TES consists of a large storage where heated operating fluid – e.g., thermal oil, molten salt, etc. – is stored for subsequent use. However, other more advanced technologies can be used to improve storage performance. For instance, Pourmoghadam and Kasaeian [13], analysed a phase change material (PCM) thermal storage to increase reliability and operating hours of a solar-based MSG, which included absorption refrigeration cycle (ARC), multi-effect distillation (MED), ejector cooling cycle (ERC), and Organic Rankine cycle (ORC). The studied MGS achieved an LCOE of 0.121 US$/kWh and a 6-year pay-back period.

Another example of subsystems that can be coupled into a solar-powered MSGs is represented by desalination processes for potable water production, which is particularly relevant for arid regions where the availability of fresh and clean water for agriculture or human consumption is relatively scarce. This topic has attracted a lot of interest over the last decade, mainly aimed at identifying the best technology solutions to produce fresh water [14] to increase the climate change resilience of local communities [15]. For instance, Khaleghi et al. [16] proposed an S-MGS with parabolic collectors, coupled with a CAES system to provide sustainable potable water and electric power in hot arid regions. The TES system improved efficiency by 33.5% while it was capable of producing around 2000 m^3 of potable water for 28 days while generating about 50 MW of electricity.

While previous studies have demonstrated the feasibility of solar-driven multi-generation systems, most of them focus on limited outputs such as electricity and cooling or electricity and hydrogen. These studies often neglect the potential benefits of integrating multiple utility products, particularly potable water and hydrogen, within a unified configuration. Furthermore, the environmental aspects of system operation, especially those based on exergy destruction, are frequently overlooked or only partially addressed.

In addition, although several works have included energy and economic assessments, comprehensive 4E (energy, exergy, economic, and exergo-environmental) analyses remain scarce. Most existing research lacks a detailed component-level assessment that quantifies performance trade-offs and identifies critical subsystems in terms of environmental impact and cost-effectiveness. This limitation hampers the ability to optimize system layouts for both sustainability and financial viability. Consequently, there is a clear need for studies that simultaneously address energy, water, cooling, and hydrogen production within a fully integrated solar-based system, supported by robust 4E analysis.

Consequently, there is a clear need for studies that simultaneously address electricity, potable water, cooling, and hydrogen production within a fully integrated solar-based system, supported by robust 4E analysis. There is also a lack of design approaches that evaluate sub-system interactions and their contribution to overall performance. Addressing this gap can support the development of resilient, off-grid, or grid-connected solutions in diverse climatic conditions.

To address these gaps, this study proposes a novel solar-powered multi-generation system that integrates parabolic trough collectors, thermal energy storage, ORC, ARC, PEME, and RO units. This system is assessed through a comprehensive 4E framework to provide a detailed understanding of its technical performance, economic feasibility, and environmental implications. The goal is to present a scalable and sustainable solution capable of delivering multiple essential utilities in a unified energy system.

Table 1
Specifications and main properties of the Therminol oil VP-I.

No.	Specification of Therminol oil VP-I	Details
1	Chemical Composition	Eutectic blend of biphenyl and diphenyl oxide (DPO)
2	Maximum Allowable Bulk Temperature	400 °C
3	Maximum Allowable Film Temperature	430 °C
4	Boiling Point (Normal)	257 °C

2. Materials and methods

2.1. System description

The present paper proposes an innovative MSG configuration, shown in Fig. 1, which relies on solar energy as its main source of power. Solar energy is extracted and converted into heat by a set of parabolic trough collectors (PTC) where thermal oil (*Therminol Oil VP-I*) is used as operating fluid. The main properties of the thermal oil are shown in Table 1. The system operates by harnessing sunlight to heat the operating fluid, which flows through the PTC.

A thermal storage (TES) is installed to store any excess thermal energy produced for subsequent use, e.g., during periods when sunlight is unavailable, to extend the operating hours of the plant. During the charging process, the hot Therminol Oil VP-I transfers its heat to the TES via a heat exchanger. The stored thermal energy is subsequently discharged to power other processes, including the ORC (between states 10 to 11 in Fig. 1). Once heated, the Therminol Oil VP-I heats the working fluids inside the evaporator of an Organic Rankine Cycle (ORC) (states 10, 11) and in an Absorption Refrigeration Cycle (ARC) generator (states 8, 2). Isobutane is used in the ORC as an operating fluid, while the working fluid in the ARC is a water-lithium bromide solution.

The ORC system consists of a circulating pump (Pump II: states 9, 10), which raises the pressure of the ORC working fluid up to the cycle maximum pressure before entering the evaporator, where it changes phase from compressed liquid to superheated vapour (states 10 to 11). Then, the fluid enters the ORC expander where mechanical energy is generated (states 11 to 12), and then converted into electricity by a generator. Then, the low-pressure vapour enters in a condenser heat exchanger where it is condensed, exiting as saturated liquid (states 9, 12 to 14), where heat is released to a cooling water circuit.

Part of the electricity generated by the ORC sub-system is delivered to the end-user, while the remaining is used to operate the pumps, a reverse osmosis (RO), and the electrolyzer units. The RO system extracts seawater to produce potable water, while the brine resulting from the process is processed and disposed of to limit its environmental impact (states 1, 15, and 16). Potable water can be used for human consumption and for extracting hydrogen into the electrolyzer (states 20 to 23). The hydrogen produced is stored as a clean fuel source for later use, while the oxygen can either be vented or utilized in industrial applications.

Table 2 shows a detailed breakdown of each assumption used in mathematical modelling for all S-MSG sub-systems considered.

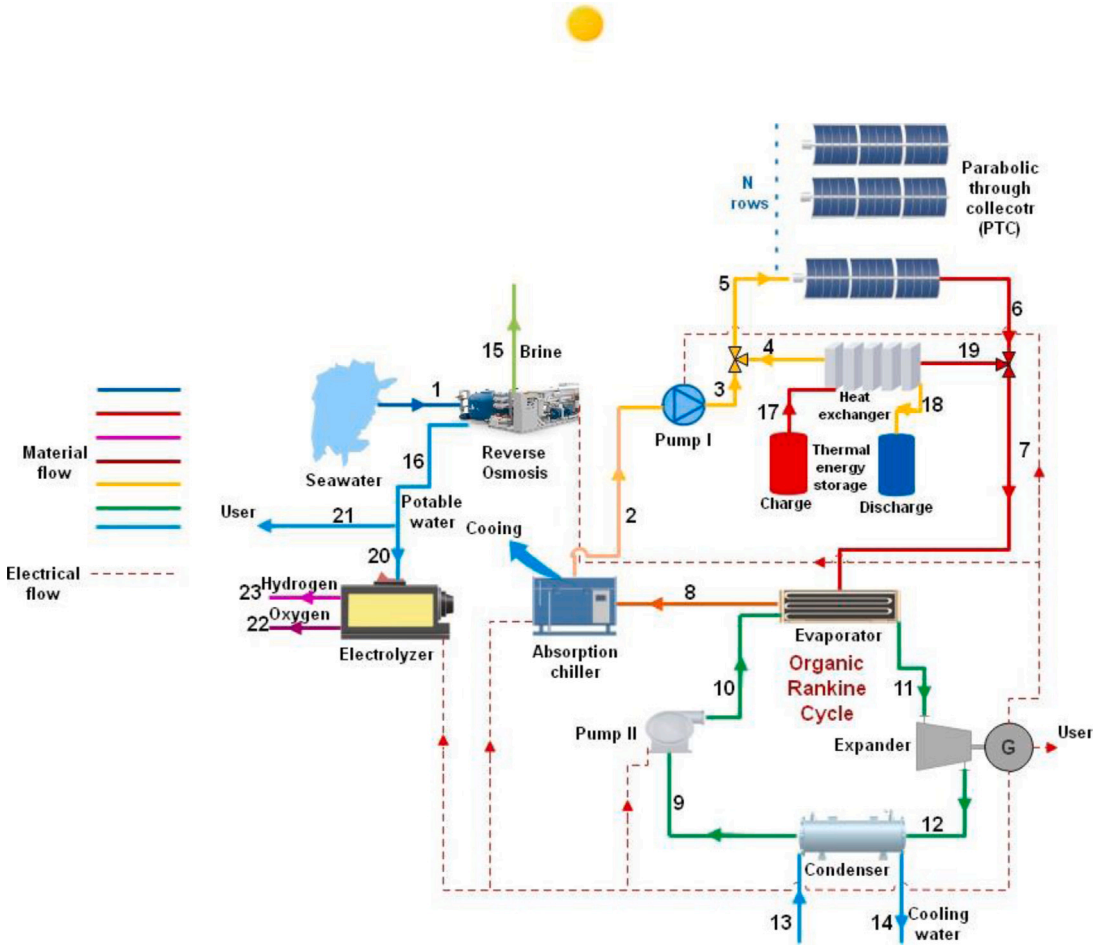

Fig. 1. The schematic illustration of the MGS.

2.2. Thermodynamic modelling

2.2.1. Parabolic through collector

The PTC subsystem model is based on the work presented in Al-Sulaiman et al. [17] where the PTC usable energy rate is determined as follows:

$$\dot{Q}_u = \dot{m}_{re}\left(c_o T_o - c_i T_i\right) \tag{1}$$

where $\dot{Q}_u$ indicates the useful energy output, while $\dot{m}_{re}$ represents the mass flow rate. The terms T and c indicates the temperature and the specific heat capacity respectively, while subscripts *re* corresponds to the receiver and subscripts *i* and *o* indicate the inlet and outlet conditions of the receiver, respectively. Another approach for calculating $\dot{Q}_u$ is based on the equation below:

$$\dot{Q}_u = A_{ap} F_R \left(S - \frac{A_{re}}{A_{ap}} U_L (T_i - T_o)\right) \tag{2}$$

where S, A_{ap}, and F_R are the quantity of radiation absorbed by the receiver, the collector aperture area, and the heat removal factor, respectively. The receiver area is denoted by A_{re}, while the PTC total heat loss coefficient is represented by U_L. The aperture area can be computed as:

$$A_{ap} = \left(w - D_{oc}\right) L \tag{3}$$

where L and D_{oc} define the PTC length and the outer cover diameter, respectively, while the term w denotes the overall width of the collector. The amount of radiation captured by the PTC is given by:

$$S = G_b \eta_r \tag{4}$$

where G_b is the solar radiation and η_r denotes the solar collector efficiency, which can be computed as:

$$\eta_r = \rho_c \gamma \tau \alpha K_\gamma \tag{5}$$

The terms α, K_γ, γ, τ, and ρ_c are the receiver absorbance, incidence angle modifier, intercept factor, glass cover transmittance, and mirror reflectance respectively. Finally, the heat removal factor can be computed as:

$$F_R = \frac{\dot{m}_{re} c_{HTF}}{A_{re} U_L}\left(1 - \exp\left(\frac{-A_{re} U_L F_1}{\dot{m}_{re} c_{HTF}}\right)\right) \tag{6}$$

Subscript *HTF* in Eq. (6) denotes the heat transfer fluid, while F_1 indicates the collector efficiency factor, determined as:

$$F_1 = \frac{U_{ar}}{U_L} \tag{7}$$

Then, the PTC thermal energy loss coefficient is:

$$U_L = \left(\frac{A_{re}}{\left(h_{cca} + h_{rca}\right) A_c} + \frac{1}{h_{rcr}}\right)^{-1} \tag{8}$$

where h_{cca} and h_{rca} represent the convective and radiation heat transfer coefficients, respectively. The convective heat transfer coefficient is given by:

$$h_{cca} = \frac{Nu_{ca} k_{air}}{D_{oc}} \tag{9}$$

where k denotes heat conduction coefficient. The Nusselt number Nu_{ca} in Eq. (9) can be calculated by using the following correlations, as

Table 2
Key assumptions and their justifications for the system modelling.

No.	Assumptions	Justification and Explanation
1	Reference environment conditions (Temperature: 25 °C, Pressure: 1 atm)	These are standard ambient conditions used in thermodynamic simulations and exergy analysis. They allow consistent comparison and benchmark calculations across various scenarios.
2	Polytropic processes for pumps and expander (Efficiency: 80%)	Polytropic models reflect real device behaviour more accurately than isentropic assumptions. An efficiency of 80% is typical for mid-scale thermal and fluid systems.
3	Neglecting potential and kinetic energies	Variations in height and velocity are negligible compared to thermal and pressure energy. This simplifies the energy and exergy balance equations without significant loss of accuracy.
4	Pressure losses in pipes (3% in each connection pipe)	A pressure drop of 3% per pipe segment is assumed to account for friction and minor losses, which affect system pressure levels and energy consumption.
5	Heat exchanger effectiveness (Effectiveness: 80%)	An effectiveness of 80% means that 80% of the maximum possible heat transfer occurs. This is a realistic value for typical industrial heat exchangers.
6	RO system recovery ratio (Recovery ratio: 30%)	This refers to the portion of feedwater converted into potable water. A 30% recovery ratio is realistic for seawater desalination with acceptable membrane performance and energy use.
7	Pinch point temperature (10 °C)	A 10 °C pinch point is selected to ensure sufficient temperature difference for heat transfer while maintaining compact heat exchanger design.
8	COP for the Absorption Chiller (COP = 0.78)	A coefficient of performance of 0.78 is based on typical values for single-effect LiBr-water absorption chillers driven by low- to medium-temperature heat sources.
9	Constant solar irradiance input (Nominal: 800 W/m^2)	A constant value of 800 W/m^2 represents average solar conditions during peak sunshine. While real solar input fluctuates, thermal storage compensates for this in the model.

suggested by Hurst [18]:

$$Nu_{ca} = C Re_{ca}^{m} Pr_{a}^{n} \left(\frac{Pr_a}{Pr_c} \right) \tag{10}$$

where Re represents the Reynolds number, Pr is the Prandtl number, and C, m, and n are constants. The radiation heat transfer coefficient in Eq. (8) can be calculated as shown in the equation below:

$$h_{rca} = \epsilon_{ac} \sigma \left(T_c + T_a \right) \left(T_c^2 + T_a^2 \right) \tag{11}$$

where σ is the Stefan–Boltzmann constant, and ϵ is the surface emittance. The radiation heat coefficient between the receiver and cover is given by:

$$h_{rcr} = \frac{\sigma \left(T_c + T_{r,av} \right) \left(T_c^2 + T_{r,av}^2 \right)}{\frac{1}{\epsilon_r} + \frac{A_r}{A_c} \left(\frac{1}{\epsilon_{r,c-1}} \right)} \tag{12}$$

Finally, the PTC energy efficiency is defined as:

$$\eta_{PTC} = \frac{\dot{Q}_u}{N_{PTC} A_{ap} G_b} \tag{13}$$

where N_{PTC} denotes the number of PTC rows and N_{PTC} can be calculated as follows:

$$N_{\mathrm{PTC}} = \lfloor \frac{\dot{m}_5}{\dot{m}_r} \rfloor + 1 \tag{14}$$

2.2.2. Thermal energy storage

The performance of the TES unit can be analysed using the quasi-dynamic technique and the finite-time thermodynamics (FTT) method. FTT evaluates the operation of energy systems under real-world constraints, such as process irreversibilities, heat losses, and time-dependent variations of main parameters. The thermal energy required for operating the ORC expander is defined as [19,20]:

$$E_{\mathrm{RES}} = \frac{t_d \left(\dot{W}_{\mathrm{ex}} \right)}{\eta_{\mathrm{en}}} \tag{15}$$

$$E_{\mathrm{ES}} = \frac{t_c \left(\dot{W}_{\mathrm{ex}} \right)}{\eta_{\mathrm{en}}} \tag{16}$$

where t denotes operating time, subscripts d and c indicate discharge and charge modes, respectively, and subscript ex denotes expander. The mass flow rate of Therminol VP-I is determined as follows:

$$\dot{m}_{oil} = \frac{E_{ES}}{t_c \Delta h_{max}} \tag{17}$$

$$\dot{m}_{oil.d} = \frac{E_{RES}}{t_d \Delta h_{max}} \tag{18}$$

The highest possible enthalpy difference, $\Delta h_{\max}$, corresponds to the highest temperature increase in the temperature of the mineral oil, which may range from a maximum of 573 K to a minimum of 473 K [19]. Therefore, the total required mass to operate the ORC expander is defined as follows:

$$\dot{m}_{oil.d} = \frac{E_{RES}}{t_d \Delta h_{max}} \tag{19}$$

$$m_{oil.d} = \dot{m}_{oil.d} \cdot t_d \tag{20}$$

$$m_{oil} = \dot{m}_{oil} \cdot t_c \tag{21}$$

The volume of the hot and cold storage tanks can be expressed as follows:

$$V_{tank} = \frac{E_{ES}}{\rho_{oil}\left(h_{17} - h_{18}\right)} \tag{22}$$

where ρ represents the density. The energy balance for the hot and cold storage tanks during the charging process can be expressed as follows:

$$Q_{\text{in-TES}} - Q_{\text{loss,ch}} = Q_{\text{ch}} \tag{23}$$

$$Q_{\text{in-TES}} - Q_{\text{loss,cd}} = Q_{\text{cd}} \tag{24}$$

$Q_{\text{in-TES}}$, $Q_{\text{loss.ch}}$, and $Q_{\text{loss.cd}}$ correspond to the net thermal energy delivered to the hot and cold tanks, along with the thermal energy losses from these tanks, respectively. The energy stored in the tanks during the charging and discharge phases is represented by Q_{ch} and Q_{cd}. The following relations calculate the energies stored in the hot and cold tanks:

$$Q_{ch} = m_{oil}\left(h\left(T_{ch}\right) - h\left(T_{ic}\right)\right) \tag{25}$$

$$Q_{cd} = m_{oil}\left(h\left(T_{cd}\right) - h\left(T_{id}\right)\right) \tag{26}$$

The net thermal energy is calculated as follows:

$$Q_{\text{in-TES}} = Q\eta_{\text{hx}} \tag{27}$$

where η_{hx} represents the heat exchanger effectiveness factor. Heat losses are calculated using the following relations:

$$Q_{\text{loss.ch}} = U A_{\text{tank}}\left(T_{\text{ch}} - T_o\right) t_c \tag{28}$$

$$Q_{\text{loss.cd}} = U A_{\text{tank}}\left(T_{\text{cd}} - T_o\right) t_c \tag{29}$$

Here, U represents the overall heat transfer coefficient, and A denotes the effective heat transfer area in the heat exchangers. For hot and cold storage tanks functioning in discharge mode, the first law of thermodynamics is expressed as follows:

$$Q_{\text{out-TES.h}} + Q_{\text{loss.dh}} = Q_{\text{ch}} \tag{30}$$

$$Q_{\text{out-TES.c}} + Q_{\text{loss.dc}} = Q_{\text{cd}} \tag{31}$$

where the thermal energy loss from the storage tanks is represented by Q_{loss}. The total thermal energy recovered from the hot and cold storage tanks is denoted by $Q_{\text{out-TES.h}}$ and $Q_{\text{out-TES.c}}$, which are calculated by using the following relations:

$$Q_{\text{out-TES.h}} = m_{\text{oil.d}}\left(h(T_{\text{ch}}) - h(T_{\text{dh}})\right) \tag{32}$$

$$Q_{\text{out-TES.c}} = m_{\text{oil.d}}\left(h(T_{\text{cd}}) - h(T_{\text{dd}})\right) \tag{33}$$

where, in the discharging mode, T_{dh} and T_{dd} display the hot and cold storage tanks final temperatures. The definition of thermal energy loss is:

$$Q_{\text{loss.dh}} = U A\left(T_{\text{dh}} - T_o\right) t_d \tag{34}$$

$$Q_{\text{loss.dc}} = U A\left(T_{\text{dd}} - T_o\right) t_d \tag{35}$$

The following relation is used to determine the energy balance of the heat exchanger during the discharging process:

$$\dot{m}_4 h_4 + \dot{m}_{\text{oil.d}} h(T_{\text{dh}}) = \dot{m}_{19} h_{19} + \dot{m}_{\text{oil.d}} h(T_{\text{dd}}) \tag{36}$$

Table 3
Mass and energy balance relations for ORC components and pump I.

No.	Component	Mass balance	Energy balance
1	Pump II	$\dot{m}_9 = \dot{m}_{10}$	$\dot{W}_{\text{pump II}} = \dot{m}_9(h_{10} - h_9)$
2	Expander	$\dot{m}_{11} = \dot{m}_{12}$	$\dot{W}_{\text{expander}} = \dot{m}_{11}(h_{11} - h_{12})$
3	Evaporator	$\dot{m}_7 = \dot{m}_8,\ \dot{m}_{10} = \dot{m}_{11}$	$\dot{m}_7\left(h_7 - h_8\right)\eta_{\text{HX}} = \dot{m}_{10}(h_{11} - h_{10})$
4	Condenser	$\dot{m}_9 = \dot{m}_{12},\ \dot{m}_{13} = \dot{m}_{14}$	$\dot{m}_9\left(h_{12} - h_9\right)\eta_{\text{HX}} = \dot{m}_{13}(h_{14} - h_{13})$
5	Pump I	$\dot{m}_2 = \dot{m}_3$	$\dot{W}_{\text{pump I}} = \dot{m}_2(h_3 - h_2)$

2.2.3. Organic Rankine cycle

The thermodynamic model of the ORC system is based on the energy balance of each system components which are shown in Table 3 [21].

The ORC net power output and efficiency can be computed as follows:

$$\dot{W}_{\text{net,ORC}} = \dot{W}_{\text{expander}} - \dot{W}_{\text{pump},II} \tag{37}$$

$$\eta_{\text{en}} = \frac{\dot{W}_{\text{net,ORC}}}{\dot{m}_7\left(h_7 - h_8\right)} \tag{38}$$

2.2.4. Reverse osmosis

The reverse osmosis subsystem is modelled based on mass and concentration balance relations [22–25], which re reported in the equations here below:

$$\dot{m}_{\text{SW}} = \dot{m}_{\text{BW}} + \dot{m}_{\text{PW}} \tag{39}$$

$$\dot{m}_{\text{SW}} x_{\text{SW}} = \dot{m}_{\text{PW}} x_{\text{PW}} + \dot{m}_{\text{BW}} x_{\text{BW}} \tag{40}$$

where x is the concentration of salt, while the subscripts PW, SW, and BW indicate potable water, seawater, and brain water. The following relation determines the relationship between seawater and potable water:

$$\dot{m}_{\text{PW}} = RR \cdot \dot{m}_{\text{SW}} \tag{41}$$

where the recovery ratio is denoted by RR. The three primary streams osmosis pressures are determined as follows [22–25]:

$$\pi_{\text{SW}} = RT \times x_{\text{SW}} \tag{42}$$

$$\pi_{\text{PW}} = RT \times x_{\text{PW}} \tag{43}$$

$$\pi_{\text{BW}} = RT \times x_{\text{BW}} \tag{44}$$

where the universal gas constant is denoted by the term R. Then, the membrane net pressure and the water permeability coefficient can be calculated as follows:

$$\Delta\pi = \left(\frac{\pi_{\text{SW}} + \pi_{\text{BW}}}{2}\right) - \pi_{\text{PW}} \tag{45}$$

$$K_W = \frac{6.84 \times 10^{-8}\left(18.68 - 0.177 x_{\text{BW}}\right)}{T_{\text{SW}}} \tag{46}$$

The RO pump's net pressure is established by:

$$\Delta P = \frac{\dot{m}_{\text{PW}}}{K_W A_m} + \Delta\pi \tag{47}$$

where the membrane area is denoted by A_m. The RO pump power requirements are computed as:

$$\dot{W}_{P,\text{RO}} = \frac{\Delta P\, \dot{m}_{\text{SW}}}{\rho_{\text{SW}}\, \eta_{P,\text{RO}}} \tag{48}$$

The storage tank volume of the RO system is calculated as [26–28]

$$V_{\text{Tank}} = \frac{\left(\dot{m}_{\text{PW}}/\text{RO}\right) \cdot t_{\text{storage}}}{f_{\text{usable}}} \tag{49}$$

Finally, the energy efficiency of the RO subsystem can be calculated by:

$$\eta_{\text{energy,RO}} = \frac{\dot{m}_{16} h_{16}}{\dot{W}_{\text{dot,RO}} + \dot{m}_1 h_1} \tag{50}$$

where t_{storage} denotes the daily discharging time of the tank, f_{usable} represents the usable fraction of the tank capacity (between 0.5 and 0.8).

2.2.5. Proton exchange membrane electrolyzer (PEME)

The required amount of energy for operating the PEME unit is determined by the following relation [29–31]:

$$\Delta H = \Delta G + T\Delta S \tag{51}$$

where ΔG denotes the Gibbs free energy, and $T\Delta S$ denotes the thermal energy required for electrolysis. The rate of hydrogen generation can computed as [29–31]:

$$\dot{N}_{\text{H}_2\text{.out}} = \dot{N}_{\text{H}_2\text{O.reacted}} = \frac{J}{2F} \tag{52}$$

where J and F stand for the current density and the Faraday constant, respectively. The water rate that reacts during the electrolysis process is indicated by the term $\dot{N}_{\text{H}_2\text{O.reacted}}$. The electric energy required by PEME can be determined as follows:

$$E_{\text{electric}} = JV \tag{53}$$

The following relation calculates the PEME operating voltage in the previous equation:

$$V = V_0 + \eta_{\text{act.a}} + \eta_{\text{act.c}} + \eta_{\text{ohm}} \tag{54}$$

where V_0 denotes a reversible potential, defined as follows:

$$V_0 = 1.299 - 8.5 \times 10^{-4} \times \left(T_{\text{PEME}} - 298\right) \tag{55}$$

The following relationship determines the membrane local ionic conductivity:

$$\sigma\left[\lambda(x)\right] = \left[0.5139 \times \lambda(x) - 0.326\right] \exp\left[1268 \times \left(\frac{1}{303} - \frac{1}{T}\right)\right] \tag{56}$$

where x is the membrane depth, while the term $\lambda(x)$ denotes the water content at the membrane x location. The equation for $\lambda(x)$ is the following:

$$\lambda(x) = \frac{\lambda_{\text{an}} - \lambda_{\text{ca}}}{L} x + \lambda_{\text{ca}} \tag{57}$$

where the water content is indicated by λ. The cathode and anode membranes are indicated by the subscripts ca and an, respectively, while the thickness of the membrane is denoted by L. The following formula determines the total ohmic resistance:

$$R_{\text{PEME}} = \int_0^L \frac{dx}{\sigma\left[\lambda(x)\right]} \tag{58}$$

The definition of the ohmic overpotential using Ohmic law is the following:

$$\eta_{\text{ohm}} = J R_{\text{PEME}} \tag{59}$$

The overpotential for electrode activation is computed as follows:

$$\eta_{\text{act},i} = \frac{RT}{F} \sinh^{-1}\left(\frac{J}{2J_{o,i}}\right) = \frac{RT}{F} \ln\left[\frac{J}{2J_{o,i}} + \sqrt{\left(\frac{J}{2J_{o,i}}\right)^2 + 1}\right], \quad i = \text{an, ca} \tag{60}$$

The exchange current density for the PEME unit is determined using the following calculation:

$$J_{0,i} = J_i^{\text{ref}} \exp\left(-\frac{E_{\text{act},i}}{RT}\right), \quad i = \text{an, ca} \tag{61}$$

Table 4
Equations to compute the exergy destruction rate for MGS subsystems.

No.	Component	EDR formula
1	ARC	$\dot{m}_2\left(\Psi_8 - \Psi_2\right) - \dot{Q}_E\left(1 - \frac{T_0}{T_G}\right)$
2	Pump II	$\dot{m}_9\Psi_9 - \dot{m}_{10}\Psi_{10} + \dot{W}_{\text{pump,II}}$
3	Expander	$\dot{m}_{11}\Psi_{11} - \dot{m}_{12}\Psi_{12} - \dot{W}_{\text{expander}}$
4	Evaporator	$\dot{m}_7\left(\Psi_7 - \Psi_8\right) + \dot{m}_{10}\left(\Psi_{10} - \Psi_{11}\right)$
5	Condenser	$\dot{m}_{20}\left(\Psi_{12} - \Psi_9\right) + \dot{m}_{13}\left(\Psi_{13} - \Psi_{14}\right)$
6	HX	$\dot{m}_{17}\Psi_{17} + \dot{m}_4\Psi_4 - \dot{m}_{19}\Psi_{19} - \dot{m}_{18}\Psi_{18}$
7	Pump I	$\dot{m}_2\Psi_2 - \dot{m}_3\Psi_3 + \dot{W}_{\text{pump,I}}$
8	PEME	$\dot{m}_{20}\Psi_{20} - \dot{m}_{22}\Psi_{22} - \dot{m}_{23}\Psi_{23} + \dot{W}_{\text{PEME}}$
9	RO	$\dot{m}_1\Psi_1 - \dot{m}_{15}\Psi_{15} - \dot{m}_{16}\Psi_{16} + \dot{W}_{\text{RO}}$
10	PTC	$\left(\dot{m}_5\Psi_5 - \dot{m}_6\Psi_6\right) + A_{ap} N_{PTC} G_b\left(1 - \frac{4}{3}\left(\frac{T_0}{T_{\text{sun}}}\right) + \frac{1}{3}\left(\frac{T_0}{T_{\text{sun}}}\right)^4\right)$

In this equation, J_i^{ref} represents the pre-exponential factor, while $E_{\text{act},i}$ refers to the activation energy. The following equation can be used to calculate the energy efficiency of the PEME subsystem:

$$\eta_{\text{energyPEME}} = \frac{\dot{m}_{23} \cdot \text{LHV}_{\text{H}_2}}{\dot{W}_{\text{PEME}} + \dot{m}_{20} \cdot h_{20}} \tag{62}$$

2.2.6. Absorption refrigeration cycle

The overall efficiency of the absorption refrigeration cycle can be calculated as shown below [32]:

$$\text{COP} = \frac{\dot{Q}_E}{\dot{Q}_G} \tag{63}$$

where $\dot{Q}$ indicates the heat transfer rate, while the subscripts E and G denote the evaporator and generator of the ARC. In the present work, the COP of the ARC subsystem is assumed to be equal to 0.8, which is the average COP among commercial ARC system [32]. Starting from this assumption, the term $\dot{Q}_G$ is calculated as shown in the equation below:

$$\dot{Q}_G = \eta_{\text{HX}}\left(\dot{m}_8 h_8 - \dot{m}_2 h_2\right) \tag{64}$$

2.2.7. Multi generation system

The net power produced by the MGS can be determined as follows:

$$\dot{W}_{\text{net,MGS}} = \eta_G \dot{W}_{\text{expander}} - \sum_{i=1}^{2} \dot{W}_{\text{pump},i} - \dot{W}_{\text{PEME}} - \dot{W}_{\text{RO}} \tag{65}$$

The subscript G denotes generator. Then, the overall energy efficiency of the MGS is determined by the following relation:

$$\eta_{\text{en}} = \frac{\dot{W}_{\text{net,MGS}} + \dot{Q}_E + \dot{m}_{21} h_{21} + \dot{m}_{23}\text{LHV}_{\text{H}_2}}{N_{\text{PTC}} A_{\text{ap}} G_b + \dot{m}_1 h_1} \tag{66}$$

2.3. Exergy analysis

Generally, specific exergy (Ψ) can be categorized into four types: chemical, kinetic, physical, and potential. Each of these categories illustrates a unique way in which a system or substance can conduct work in connection to its surroundings [33,34]. This concept can be expressed mathematically as shown below:

$$\Psi = \sum x_i \Psi_{\text{chi}} + \frac{V^2}{2} + gz + \left(h - h_0\right) - T_0\left(s - s_0\right) + T_0 \sum x_i R_i \ln y_i \tag{67}$$

where x is the mass fraction is represented, while subscripts 0, i, and ch indicate the dead state, the species, and the chemical exergy, respectively. The terms, g, V, and z correspond to gravitational acceleration, velocity, and height, respectively. Additionally, y and s refer to the mole fraction and specific entropy. The exergy destruction rate (EDR) for every MGS component and subsystem is shown in Table 4.

The exergy efficiency (η_{ex}) relations for subsystems are reported here below:

$$\eta_{\text{ex,ORC}} = \frac{W_{\text{net, ORC}}}{\dot{m}_7(\Psi_7 - \Psi_8)} \tag{68}$$

$$\eta_{ex,\ \mathrm{ARC}} = \frac{\dot{Q}_E\left(1-\frac{T_0}{T_G}\right)}{\dot{m}_2\left(\Psi_8-\Psi_2\right)} \tag{69}$$

$$\eta_{ex,\ \mathrm{RO}} = \frac{\dot{m}_{16}\Psi_{16}}{\dot{m}_1\Psi_1+\dot{m}_{15}\Psi_{15}+\dot{W}_{\mathrm{RO}}} \tag{70}$$

$$\eta_{ex,\ \mathrm{PEME}} = \frac{\dot{m}_{23}\Psi_{23}}{\dot{m}_{20}\Psi_{20}+\dot{W}_{\mathrm{PEME}}} \tag{71}$$

$$\eta_{ex,\ \mathrm{PTC}} = \frac{\left(\dot{m}_5\Psi_5-\dot{m}_6\Psi_6\right)}{G_b A_{ap} N_{PTC}\left(1-\frac{4}{3}\left(\frac{T_0}{T_{\mathrm{sun}}}\right)+\frac{1}{3}\left(\frac{T_0}{T_{\mathrm{sun}}}\right)^4\right)} \tag{72}$$

$$\eta_{ex,\ \mathrm{MGS}} = \frac{\dot{Q}_E\left(1-\frac{T_0}{T_G}\right)+\dot{W}_{\mathrm{net,\ MGS}}+\dot{m}_{23}\Psi_{23}+\dot{m}_{21}\Psi_{21}}{G_b A_{ap} N_{PTC}\left(1-\frac{4}{3}\left(\frac{T_0}{T_{\mathrm{sun}}}\right)+\frac{1}{3}\left(\frac{T_0}{T_{\mathrm{sun}}}\right)^4\right)+\dot{m}_1\Psi_1} \tag{73}$$

2.4. Exego-environmental analysis

Exergo-environmental analysis combines principles of environmental impact and exergy analysis to assess and quantify the environmental impacts caused by exergy destruction. This method examines how irreversibilities occurring in real energy systems cause resource depletion and environmental damage, offering a deeper insight into the sustainability of a system. The exergo-environmental factor is introduced to evaluate the relation between environmental damage and exergy destruction for a process or system. This parameter can be calculated by the following equation [35–37]:

$$f_{ei} = \frac{\mathrm{EDR}}{\sum \dot{m}\psi} \tag{74}$$

A system environmental damage effectiveness (EDE) factor, assesses the damage that system energy destruction rate (EDR) causes to the environment by finding a relation between energy inefficiencies and environmental impact. It can be written as [35–37]:

$$\phi_{ei} = \frac{f_{ei}}{\eta_{ex}} \tag{75}$$

The exergy stability factor (ESF) evaluates the EDR and exergy output balance. This index in exergo-environmental analysis shows what share of input exergy has been converted into output exergy (useful energy) and how much of it has been destroyed. The purpose of the number 1 in this equation is for normalization. The lower this value is, the better it is from the exergo-environmental point of view. The optimal state of this index is zero. It can be calculated by [35–37]:

$$f_{es} = \frac{\mathrm{EDR}}{\sum \dot{m}\psi_{\mathrm{xtot,out}}+\mathrm{EDR}+1} \tag{76}$$

2.5. Economic analysis

The MGS annual income cash flow (CF) denotes the annual financial return, including revenues, incentives, and savings. The CF is computed as follows [38–41]:

$$CF = Y_{\mathrm{electrical}}k_{\mathrm{electrical}}+Y_{\mathrm{H_2}}k_{\mathrm{H_2}}+Y_{\mathrm{PW}}k_{\mathrm{PW}}+Y_{\mathrm{cooling}}k_{\mathrm{cooling}}-O\&M \tag{77}$$

where Y specifies the production per year, while k represents the market price of each product per unit in 2025, as reported in Table 5 [30,42–47]. O&M (operating and maintenance) costs are assumed to by 3% of the initial investment cost [38–40].

The expected prices of electricity, hydrogen, cooling, and potable water from now until 2050 are shown in Fig. 2 [48–53]. Considering that cooling loads are typically covered by using electricity, its future outlook has been considered linked to the trend of the electricity price. However, future price trends for potable water depend on many factors - e.g., climate change, population growth, water resource management, and technological and infrastructure developments. The complexity of these factors has prevented the provision of a comprehensive and accurate forecast of potable water prices, which is reflected in the scarce available literature. However, a review of the changes in the price of drinking water in recent years shows that this price has increased by an average of 1.5% annually. Therefore, this value has been considered for the present work [54–56].

Table 5
Market price associated with each product in 2025.

No.	Product costs	Unit	Value
1	$k_{\mathrm{electrical}}$	US$/kWh	0.20
2	k_{PW}	US$/m^3	2.80
3	k_{cooling}	US$/kWh	0.02
4	$k_{\mathrm{H_2}}$	US$/kg	8.30

Table 6
Cost functions for various components.

No	Component	Cost function (US$)	Ref
1	Pump (ORC)	$C_{\mathrm{pump}} = 1026\cdot\left(\frac{W_p}{300}\right)^{0.25}$	[31,39,57]
2	Evaporator (ORC)	$C_{\mathrm{evap}} = C_{\mathrm{base}}\cdot\left(\frac{Q}{Q_{\mathrm{ref}}}\right)^{n}\cdot F_{\mathrm{mat}}\cdot F_{\mathrm{op}}$	[58,59]
3	Expander (ORC)	$C_{\mathrm{expander}} = 2237\cdot\left(\dot{W}_{Ex}\right)^{0.41}$	[31,39,57]
4	Condenser (ORC)	$C_{\mathrm{cond}} = C_{\mathrm{base}}\cdot\left(\frac{Q}{Q_{\mathrm{ref}}}\right)^{n}\cdot F_{\mathrm{mat}}\cdot F_{\mathrm{op}}$	[58,59]
5	Pump (Thermal Oil)	$C_{\mathrm{pump,thermal}} = 3540\cdot\left(\dot{W}\right)^{0.71}$	[31,39,57]
6	Pump (RO)	$C_{\mathrm{pump,RO}} = 996\cdot(86400\cdot\dot{Q})^{0.8}$	[60]
7	Membrane (RO)	$C_{\mathrm{membrane}} = 50$	[60]
8	Tank (RO)	$C_{\mathrm{tank}} = 1.14\cdot(158.62\cdot V_{\mathrm{Tank}}+18321)$	[60]
9	ARC	$C_{\mathrm{ARC}} = 1144.3\cdot\left(\dot{Q}_E\right)^{0.67}+3.3$	[60]
10	PTC and Working Fluid	$C_{\mathrm{PTC}} = 1500\cdot\dot{A}_{\mathrm{ap.total}}$	[31,39,57]
11	PEME	$C_{\mathrm{PEME}} = 1000\cdot\left(\dot{W}_{\mathrm{PEME}}\right)$	[31,39,57]
12	TES	$C_{\mathrm{TES}} = 25\cdot Q_{\mathrm{TES}}$	[31,39,57]

The total investment cost of the proposed system can be determined as shown in the following equation: [38–40]

$$C_0 = K_{\mathrm{ORC}}+K_{\mathrm{PTC}}+K_{\mathrm{RO}}+K_{\mathrm{PEME}}+K_{\mathrm{ARC}}+K_{\mathrm{TES}} \tag{78}$$

where K represents the investment cost of each subsystem. Table 6 outlines the cost function for each component and subsystem of the proposed configuration.

Regarding the ORC evaporator and condenser, the term C_{base} in Table 6 indicates a baseline cost of the component referred to a nominal heat transfer rate (Q_{ref}), while n is a cost scaling factor (evaporator: between 0.6 and 0.8; condenser: between 0.65 and 0.75). Moreover, the term F_{mat} is the factor of material related to the type of material used (evaporator: stainless steel = 1.5, carbon steel = 1.0, titanium = 2.0; condenser: stainless steel = 1.3, carbon steel = 1.0, titanium = 1.8), while F_{op} is the operating factor, considering the temperature, pressure, and complexity of operation (evaporator: low pressure = 1.0, moderate pressure = 1.2, high pressure = 1.5; condenser air-cooled = 1.2, water-cooled = 1).

The impact of the inflation rate can be considered by using the following relation : [42,43]

$$C_n = C_0(1+i)^n \tag{79}$$

where i denotes the inflation rate (2.5%), while n represents the years of operation. This inflation rate is considered for investment costs only if the cost functions refer to a specific year in the past to adjust the total capital expenditure to today's actual values.

Several indexes are introduced to evaluate the investment suitability of the proposed solution. First, the pay-back period (PP) calculates the time required for reaching the break-even, which can be computed as [42,43]:

$$PP = \frac{\ln\left(\frac{\sum_{j=1}^{N}\frac{CF_j}{(1+r)^j}}{\sum_{j=1}^{N}\frac{CF_j}{(1+r)^j}-r\cdot C_n}\right)}{\ln(1+r)} \tag{80}$$

where r represents the discount factor (6%) [61–63].

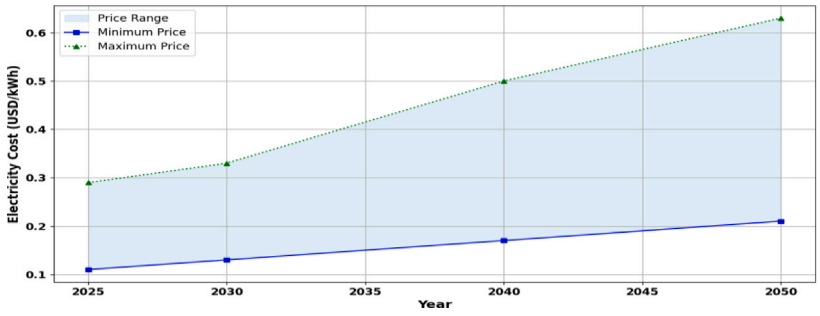

(a) Electricity

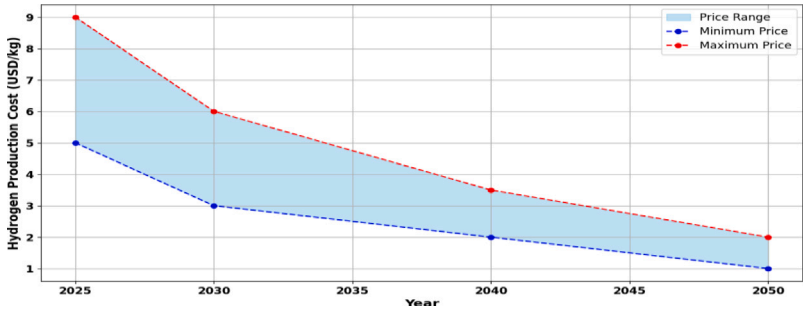

(b) Hydrogen

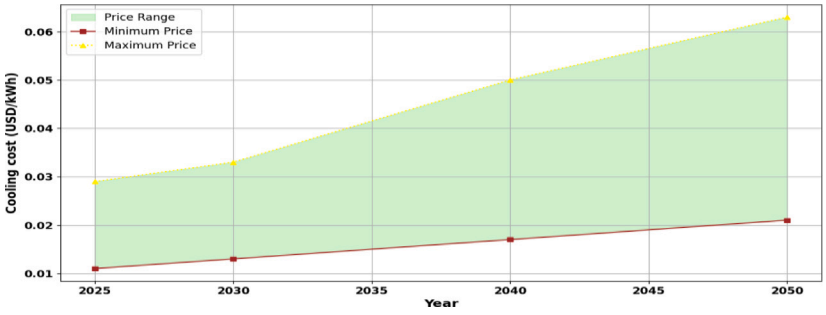

(c) Cooling

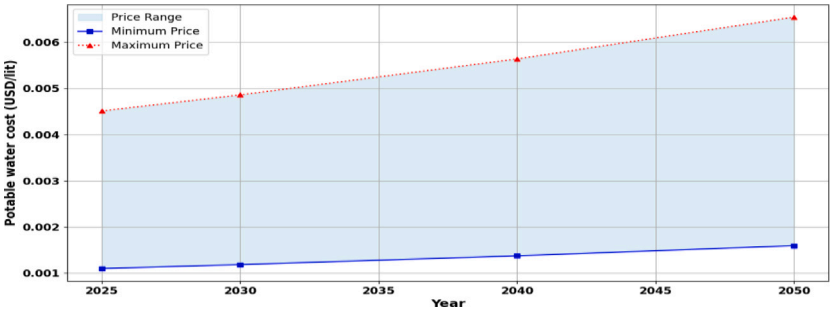

(d) PW

Fig. 2. Forecasted Trends in electricity, Hydrogen, cooling, and potable water costs from Now Until 2050.

Table 7
The input data for the developed computer program.

No.	Symbols	Definition	Value	Unit
1	x_p	Salt concentration in product water	150	mg/l
2	A_m	Effected area of membrane surface	35	m^2
3	$\dot{m}_1$	Seawater mass flow rate	1	kg/s
4	RR	Recovery ratio	0.3	–
5	T_1	Seawater temperature	298.15	K
6	T_{15}	Brine temperature	298.15	K
7	T_{16}	Potable water temperature	298.15	K
8	$\dot{m}_{10}$	Outlet of pump II mass flow rate	3	kg/s
9	P_{12}	Outlet of expander pressure	400	kPa
10	P_{10}	Inlet pressure of evaporator	1400	kPa
11	P_7	Outlet pressure of TES and PTC	303	kPa
12	T_2	Outlet temperature of ARC	313.5	K
13	D_2	Inner diameter of the absorber	0.04	m
14	D_3	Outer diameter of the absorber	0.05	m
15	D_4	Inner diameter of the glass envelope	0.087	m
16	D_5	Outer diameter of the glass envelope	0.09	m
17	G_b	Solar irradiation	2	kW/m^2
18	L	Membrane thickness	100	μm
19	W	Width of the collector	3.5	m
20	u_a	Wind speed	5	m/s
21	ρ_c	Reflectance of the mirror	0.931	–
22	γ	Intercept factor	0.93	–
23	τ	Transmittance of the glass cover	0.94	–
24	α	Absorbance of the receiver	0.94	–
25	$\dot{m}_r$	Flow rate of the HTF	0.32	kg/s
26	t_d	Discharge time	14 400	s
27	t_c	Charge time	10 800	s
28	T_{PEME}	Temperature of PEME	80	°C
29	$E_{act.a}$	Activation energy (anode)	76	kJ/mol
30	$E_{act.c}$	Activation energy (cathode)	18	kJ/mol
31	λ_a	Water content in anode	14	–
32	λ_c	Water content in cathode	10	–
33	J_{α}^{ref}	Reference current density (alpha)	1.7×10^3	A/m^2
34	J_c^{ref}	Reference current density (cathode)	4.6×10^5	A/m^2
35	P_{O_2}	Partial pressure of oxygen	1.0	atm
36	P_{H_2}	Partial pressure of hydrogen	1.0	atm

The NPV can be calculated by summing the discounted cash flows over the time horizon N of the investment (which is set at 25 years), and it is shown here below [42,43]:

$$NPV = -C_n + \sum_{j=1}^{N} \frac{CF_j}{(1+r)^j} \tag{81}$$

Finally, the Internal Rate of Return (IRR) refers to the discount rate r which causes the investment to break even (i.e., NPV equal to zero). It is a measure of the risk associated with the investment and it can be calculated by using the following equation [42,43]:

$$NPV = -C_n + \sum_{j=1}^{N} \frac{CF_j}{(1+IRR)^j} = 0 \tag{82}$$

2.6. Explanation of mathematical modelling

The numerical model described in the previous sections were implemented in the *Engineering Equation Solver (EES) software*, which allows the calculation of the thermodynamic properties and to conduct detailed analyses, including evaluations of energy, exergy, economic, and exergo-environmental (4E). EES enables precise 4E system performance modelling by integrating thermodynamic property databases with advanced mathematical solvers. Table 7 shows the input data and constraints adopted in the present work, such as thermodynamic states, system properties, and operational conditions [26,64]

The procedure adopted by the simulation model is based on the following steps:

- **Step 1 (Input Data Entry):** The main information and input data are defined and declared. This includes the definition of all system parameters such as thermodynamic properties, design conditions, and material properties.
- **Step 2 (RO System Power Consumption Calculation):** the reverse osmosis (RO) system is determined based on the input mass flow rate and the salinity of seawater. The code uses thermodynamic relations to estimate the power required for the desalination process, considering the high-pressure pump power production and the salt concentration in the feed water.
- **Step 3 (ORC System Modelling):** the ORC modelling is implemented based on the pressure inputs.
- **Step 4 (PTC and TES Modelling)**: This step is done by the temperature calculation, mass flow rate balancing, PTC sizing, and TES modelling.
- **Step 5 (ARC System Cooling Output)**: The ARC system is modelled using the COP equation to calculate the cooling capacity. The outlet temperature of the ARC is determined using energy balance equations,
- **Step 6 (PEME Power Consumption)**: The required amount of PW to be electrolysed into hydrogen is selected as an input. Then, the power consumption of the PEME is calculated. This involves estimating the electrical energy required for the electrolysis process under the specified operating conditions.
- **Step 7 (Advanced Analyses)**: This step includes exergy, economic and exergo-environmental analyses.

Fig. 3 displays the MGS procedure of calculation.

2.6.1. Selection procedure for ORC working fluid

One of the important aspects of this cycle is the selection of the working fluid in the ORC (R600: Isobutane). In this regard, the following aspects need to be considered:

1. Given that the pinch point in this analysis is assumed to be 10 °C, it is practically necessary that the temperature at state 10 is approximately 10 °C lower than the temperature at state 7. Therefore, the selection of the working fluid is based on the temperature of state 10, which should not exceed the critical temperature of the working fluid.
2. From a technical point of view, selecting the working fluid requires careful attention to the temperatures at states 9 and 12, which must be higher than the cooling fluid temperature (i.e., water), assumed at 15 °C, to allow for the heat transfer to occur. However, it should be noted that a large temperature difference reduces the effectiveness of the condenser, while a smaller temperature difference leads to an increase in the condenser size and, consequently, its cost.
3. In choosing the working fluid for thermal and refrigeration systems, it is necessary to pay attention to environmental considerations. Fluids with high global warming potential (GWP), if leaked into the atmosphere, can contribute to increasing global warming and intensifying the harmful effects of climate change. Also, fluids with high ozone depletion potential (ODPant aspe) cause damage to the ozone layer and make the Earth more vulnerable to harmful ultraviolet rays. Moreover, the toxicity is another important aspect to be considered regarding the potential impacts on human health and natural ecosystems. Therefore, choosing a fluid that does not have these harmful effects is necessary to protect the environment and comply with environmental standards and laws [65].

3. Result and discussion

3.1. Model validation

Since the entire system layout, consisting of the integration of multiple energy systems, has not been investigated so far, the accuracy of each subsystem model is evaluated individually.

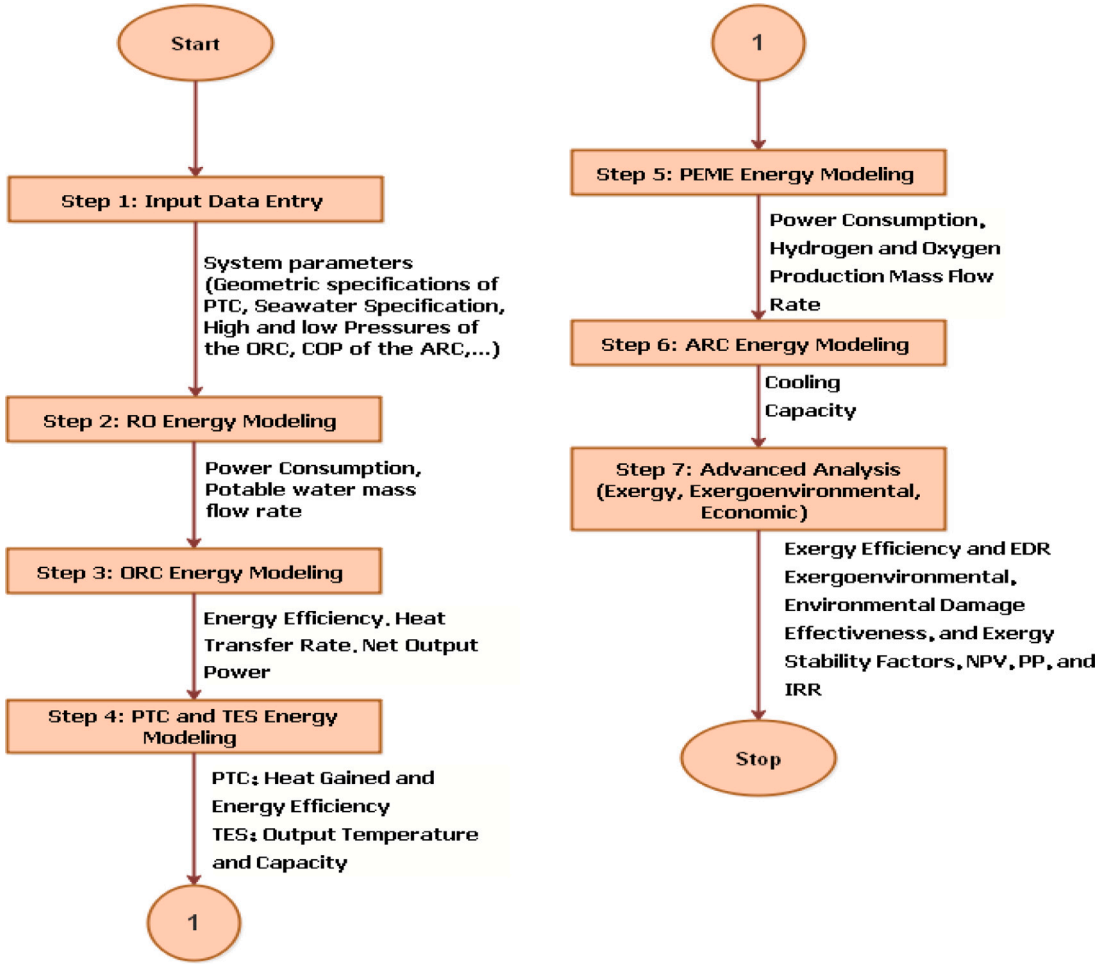

Fig. 3. Flow chart of calculation procedure.

Table 8
Comparison between the calculated data of this paper with Ref [64] for PEME validation.

No.	PEME Parameters	Cell potential (V)		Error (%)
	Current density (A/m^2)	Ref [64]	Current model	
1	0	1.2	1.2	0
2	0	1.4	1.4	0
3	0	1.6	1.6	0
4	2000	2.0	2.015	−1.5
5	3000	2.05	2.064	−1.4
6	4000	2.05	2.058	−0.8
7	5000	2.07	2.074	−0.4
8	6000	2.1	2.12	−2.0

Table 9
Comparison of ORC computer model Data with Ref. [66].

No.	ORC parameters	Computer model data	Ref. [66]	Error (%)
1	η_{en} (%)	4.5	4.6	2.2
2	$\dot{W}_{net,\ ORC}$ (kW)	517	532	2.9

Table 10
Comparison of PTC energy efficiency between Model and Ref. [67].

No.	Energy efficiency (%)	Model	Ref. [67]	Error (%)
1	10	9.7	10	3

The numerical model of the electrolyzer (PEME) subsystem is carried out by comparing its results withe the ones obtained by Ioroi et al. [64], which is shown in Table 8 where it can be noted that the deviations obtained is below 2%.

Similarly, the ORC model is validated by simulating the configuration extracted from Li et al. [66] with R245fa as working fluid. Table 9 depicts the comparison between the ORC model results and the reference data, where it can be noted that minimal deviations occurs, implying that the developed model is suitable for predicting ORC performance in terms of energy efficiency and net power production.

To validate the PTC model, the work from Dudley et al. [67] was considered. This reference is a technical report, prepared by Sandia National Laboratories, investigating the performance evaluation of the SEGS LS-2 PTC at Kramer Junction, California. Data from this reference was entered as input into the numerical model developed in the framework of the present work. Table 10 outlines the results of the comparison, showing that a good alignment between the numerical model and experimental data in terms of PTC energy efficiency is achieved, within a 3% deviation.

Finally, the reverse osmosis (RO) model was performed by comparing its results with the findings from Naseri et al. [23], which are displayed in Table 11. Since errors range from a minimum of 1.3% to a maximum of 1.7%, the accuracy of the RO numerical model is considered sufficient for carrying out a preliminary design aimed at improving RO system performance, reducing energy consumption, and designing more efficient desalination systems.

3.2. Energy and exergy analysis results

Table 12 summarizes the physical properties at various points of the MGS, offering a detailed overview of the thermodynamic parameters

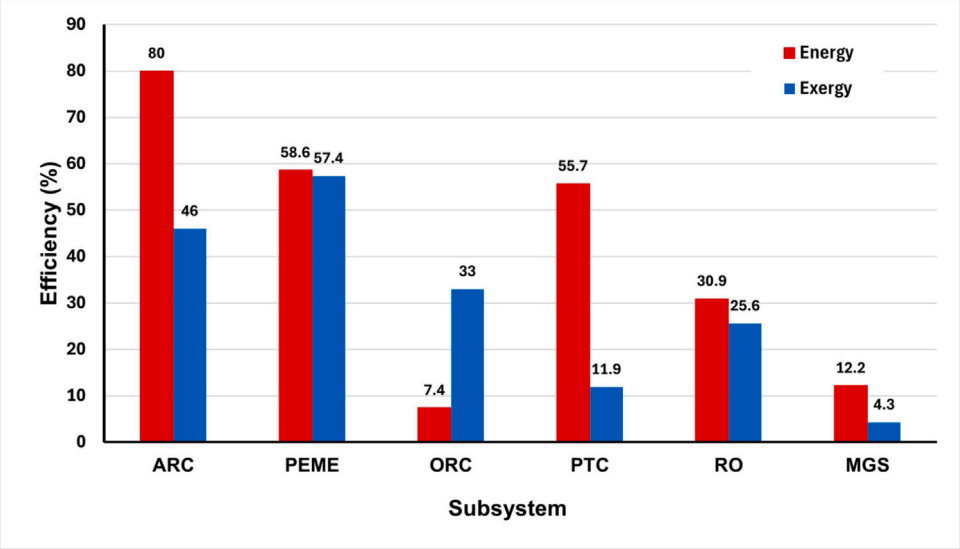

Fig. 4. Energy and exergy efficiencies for all subsystems and MGS.

Table 11
Comparison of parameters between reference and computer model for RO.

No.	Parameters	Ref. [23]	Computer model	Error (%)
1	$m_{\dot{B}W}$ (kg/s)	1.104	1.09	1.3
2	$m_{\dot{P}W}$ (kg/s)	0.456	0.448	1.7
3	$W_{\dot{P},RO}$ (kg/s)	8.96	8.8	1.7

associated with its operational performance. The table includes data on mass flow rates, pressure, temperature, specific enthalpy, entropy, and exergy. Furthermore, Table 13 shows relevant data on power production, consumption, and heat transfer rate for related components, subsystems, and MGS.

The ORC system produces 146.5 kW of net electrical power from 1576 kW of input heat rate, with low auxiliary consumptions (about 6.7 kW), showing an effective utilization of the heat generated by the PTC, making it suitable for the generation of electrical power with solar energy. The ARC provides 317 kW of cooling with about 407 kW of inlet heat rate. One unit of PTC collects around 110 kW of solar heat with minimum power consumption, showing its high utilization potential. The RO consumes 4.5 kW of electrical power for desalination, demonstrating a suitable choice for water treatment in water-scarce areas. The PEME system uses 3 kW for hydrogen production. Finally, the MGS produces 139 kW of electrical power and provides PW, cooling, and hydrogen for additional applications. Fig. 4 presents the energy and exergy efficiencies for various subsystems and MGS.

The MGS shows lower energy and exergy efficiencies (12.2% and 4.3%) than other subsystems. Although the MGS produces multiple products, its processes experience significant energy losses and a high exergy destruction rate, leading to reduced overall efficiency. The reason is related to the complex configuration of the MGS, which involves several subsystems and processes. On the other hand, the energy and exergy efficiencies of PEME are 58.6% and 57.4%, respectively, which are the highest among all subsystems. This is due to the high values of the energy content of the hydrogen produced.

Unlike other subsystems, the exergy efficiency of the ORC is higher than its energy efficiency. This is due to the smaller exergy difference between points Ψ_7 and Ψ_8 compared to the enthalpy difference h_7 and h_8. This indicates that the quality of energy is better preserved in the ORC, resulting in higher exergy efficiency compared to energy efficiency.

On the other hand, the energy efficiency of the PTC is approximately 4.7 times its exergy efficiency due to the smaller difference in specific exergy compared to the difference in enthalpy between points 5 and 6. Specific exergy, which measures the capability of a system to do useful work, is significantly reduced by irreversibilities and entropy generation occurring during each process. Ultimately, the limited difference in exergy shows the impact of these factors on system performance.

Fig. 5 illustrates the percentage distribution of the exergy destruction ratio (EDR) in each subsystem and MGS.

The highest exergy destruction rate in the MGS occurs in the PTCs, due to the large temperature difference that occurs between the source (solar radiation) and the heat collected by the thermal oil. Moreover, the high number of PTCs (32 units) arranged in parallel, while enhancing the scalability of the system, also contributes to the increase of the total EDR, including heat losses and non-ideal heat transfer processes

ORC has the second highest EDR percentage in the system. This is primarily due to the number of components within the ORC. A detailed analysis of each stage of the ORC system shows that a major portion of irreversibilities occur in the thermal oil/refrigerant heat exchangers, which is mainly due to the significant temperature difference between the thermal oil and the refrigerant in this section. Heat transfer is inherently an irreversible process and as the temperature difference between the hot and cold fluids increases, the entropy generation increases, resulting in greater exergy destruction. Since the ORC system is designed to convert thermal energy into mechanical, and then electrical energy, the presence of multiple components introduces a variety of irreversibilities, including thermal losses, friction, and inefficiencies in energy transfer, which ultimately leads to an increase in the exergy destruction rate (EDR).

The electrolyzer (PEME) shows a small percentage of the total EDR in the MGS, primarily due to its limited size and hydrogen production. However, if the mass flow rate of the incoming water (and, consequently the hydrogen production) increases, PEME exergy destruction rate will increase significantly, since the chemical process occurring in this component involves notable irreversibilities.

The low percentage of EDR of the ARC and RO is related to their small size. Smaller systems typically have lower energy flows and, consequently, lower EDR compared to larger systems. Since the EDR is directly proportional to the amount of energy transformations and losses within the system.

Also, the proposed solar-powered multi-generation system (MGS) demonstrates a high degree of adaptability for integration into existing

Table 12
Physical properties in each point of the MGS.

No.	Working fluid	$\dot{m}$ (kg/s)	P (kPa)	T (K)	h (kJ/kg)	s (kJ/kgK)	Ψ (kJ/kg)	x (–)
1	SW	1.00	101	298.2	100.5	0.354	−0.313	30,020
2	Therminol oil VP-I	10.96	285	313.2	44.0	0.146	0.734	
3	Therminol oil VP-I	10.96	312	313.2	44.1	0.146	0.760	
4	Therminol oil VP-I	0.879	312	313.2	44.1	0.146	0.760	
5	Therminol oil VP-I	10.1	312	313.2	44.1	0.146	0.760	
6	Therminol oil VP-I	10.1	303	435.1	261	0.728	44.2	
7	Therminol oil VP-I	10.96	303	435.1	261	0.728	44.2	
8	Therminol oil VP-I	10.96	294	335.8	81.1	0.261	3.75	
9	Organic fluid	3.00	400	315.1	301	1.34	37.0	
10	Organic fluid	3.00	1400	315.8	304	1.35	38.9	
11	Organic fluid	3.00	1400	415.1	829	2.78	135.7	
12	Organic fluid	3.00	400	381.4	778	2.82	74.5	
13	Water	4.97	101	288.2	63.1	0.224	132.2	
14	Water	4.97	101	343.2	293	0.955	144.5	
15	Brine	0.70	3648	298.2	101.7	0.343	4.17	42,821
16	PW	0.30	3648	298.2	108.2	0.366	3.55	150
17	Therminol oil VP-I	0.879	101	425.1	241	0.683	38.0	
18	Therminol oil VP-I	0.879	101	382.6	162	0.487	17.4	
19	Therminol oil VP-I	0.879	303	435.1	261	0.728	44.2	
20	PW	0.000131	101	298.2	104.9	0.367	0	
21	PW	0.300	101	298.2	104.9	0.367	0	
22	Oxygen	0.000117	101	353.2	50.8	0.156	4.18	
23	Hydrogen	0.000015	101	353.2	4723	55.8	65.2	

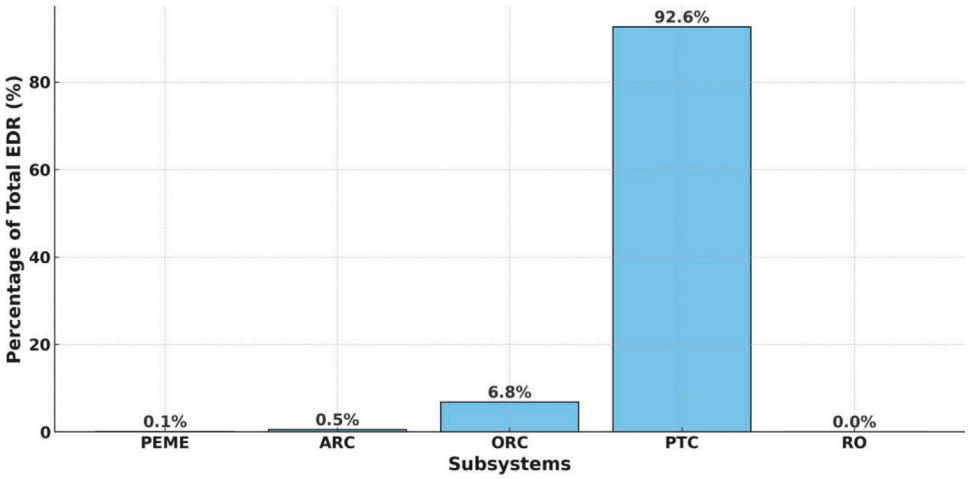

Fig. 5. Percentage distribution of the EDR in each subsystem and MGS.

Table 13
Power production, consumption, and heat transfer rate for related components, subsystems, and MGS.

No.	System	Parameter	Unit	Value
1	ORC	$\dot{Q}_{cond}$	kW	1430
2		$\dot{Q}_{ev}$	kW	1576
3		$\dot{W}_{EX}$	kW	153.3
4		$\dot{W}_{PII}$	kW	6.78
5		$\dot{W}_{ORC}$	kW	146.5
6	ARC	$\dot{Q}_E$	kW	317.2
7		$\dot{Q}_G$	kW	406.7
8	PTC	$\dot{Q}_u$	kW	110.8
9		$\dot{W}_{PI}$	kW	0.28
10		N_{PTC}	–	32
11	RO	$\dot{W}_{RO}$	kW	4.47
12	PEME	$\dot{W}_{PEME}$	kW	3
13	MGS	$\dot{W}_{MGS}$	kW	139

and future energy infrastructures. Its modular architecture facilitates connection to local or national electric grids via the ORC subsystem, supporting both on-grid and off-grid configurations. Moreover, the hydrogen produced by the PEM electrolyzer can be stored for later use or injected into hydrogen pipelines, contributing to the expansion of the hydrogen economy. The system's compatibility with other renewable technologies, including photovoltaic panels, wind turbines, and biomass units, enables its deployment in hybrid configurations, enhancing energy reliability and operational flexibility. Such interoperability makes the MGS particularly suitable for microgrid applications and decentralized energy systems in remote or underserved areas.

3.3. Exergoenvironmental analysis results

Fig. 6 illustrates the exergo-environmental factors for each subsystem and MGS. It can be noted that the electrolyzer (PEME) shows the highest f_{ei} value (0.9995), indicating that it has a substantial amount of EDR relative to its inlet exergy rate. Although PEME is highly efficient in producing hydrogen, this high f_{ei} reveals inefficiencies in its operation from an exergo-environmental point of view. Similarly, the MGS, which integrates all subsystems, exhibits a relatively high f_{ei} (94.58%). This highlights the inefficiencies of the subsystem, particularly those subsystems with higher f_{ei} values, such as PEME and ARC. The ARC subsystem shows a lower f_{ei} value (0.8802), which is the result of the conversion of the heat collected into cooling energy. Although ARC provides significant utility, it still has considerable EDR, highlighting room for improvement.

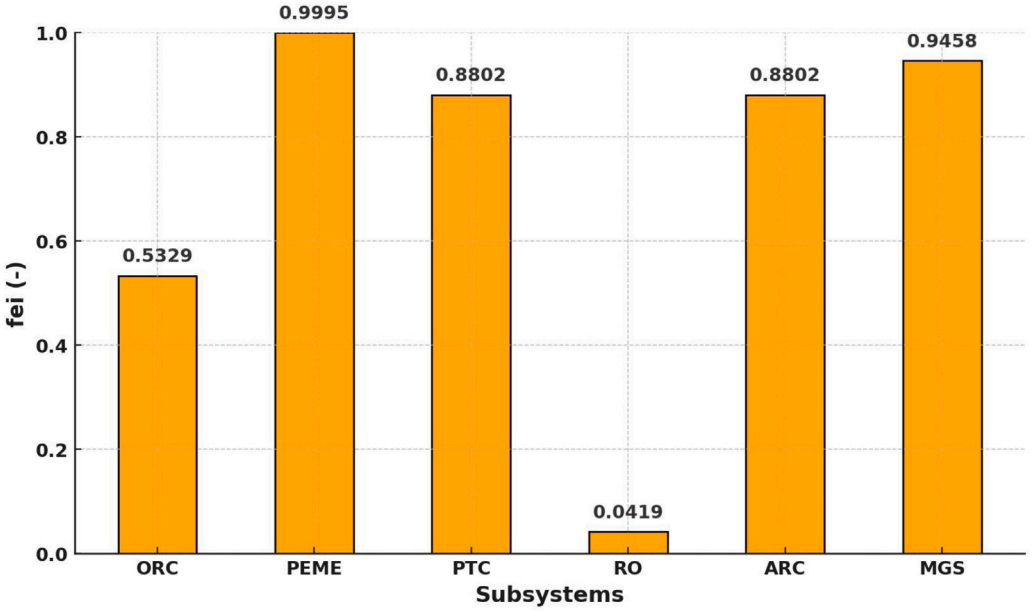

Fig. 6. Exergo-environmental factors for each subsystem and MGS.

The ORC subsystem, on the other hand, performs better than ARC, showing a lower f_{ei} value of 0.5329. This means that the ORC is comparatively more efficient in minimizing EDR relative to its inlet exergy rate. Finally, the RO subsystem is shown to be the best performing subsystem from an exergo-environmental point of view, with the lowest value f_{ei} (0.0419) due to operating near environmental conditions (dead state).

Fig. 7 illustrates the environmental damage effectiveness factor (EDE) for each subsystem and MGS. MGS exhibits the highest EDE (22.17), primarily due to its complex structure, which comprises many subsystems and components. This complexity leads to increased energy transformations and inefficiencies, which, in turn, amplify the environmental damage associated with EDR. Furthermore, the low exergy efficiency of MGS contributes further to its high EDE, as more resources are wasted and greater irreversibilities occur during operation.

At subsystem level, the reverse osmosis (RO) shows the lowest EDE (0.1637), mainly because it operates near environmental conditions. This proximity reduces thermodynamic irreversibilities and minimizes the environmental damage associated with EDR. On the other hand, ARC and ORC shows moderate EDE values (1.174 and 1.614), since their environmental impact is influenced by thermodynamic limitations and the energy used in their processes, even when powered by clean solar energy. Furthermore, with an EDE factor of 1.742, PEME has a slightly higher environmental impact, due to the energy-intensive nature of the electrolysis process, even when powered by clean energy sources like solar energy. Finally, the PTC has an EDE factor of 7.344. This value places it significantly above subsystems such as ARC, ORC, PEME, and RO, but well below MGS. The relatively high EDE factor for PTC reflects that the thermal energy conversion process in PTC systems is not entirely efficient, as energy losses occur during heat collection, transfer, and storage. These inefficiencies reduce the overall exergy efficiency of the system, contributing to its high EDE value.

Fig. 8 illustrates the exergy stability factor (ESF) factor for each subsystem and MGS. The ARC subsystem exhibits an ESF of 0.5241, indicating moderate thermodynamic stability and efficiency in converting waste solar heat into cooling energy. However, this relatively high ESF highlights significant EDR. The ORC subsystem has an ESF of 0.6158, slightly higher than ARC, indicating notable inefficiencies.

The PEME subsystem, with an ESF of 0.7497, demonstrates higher ESF compared to ARC and ORC, revealing substantial EDR. The RO subsystem stands out with an ESF of 0.0778, the lowest among all subsystems. This signifies minimal EDR relative to its exergy output and establishes it as the most efficient thermodynamically efficient subsystem. The PTC subsystem achieves an ESF of 0.8781, indicating relatively low EDR and efficient utilization of solar energy. Finally, the MGS, which integrates all subsystems, shows the highest ESF of 0.9606, reflecting the accumulated inefficiencies of the subsystems.

3.4. Economic analysis results

Fig. 9 illustrates the cost distribution of each subsystem as a percentage of the total cost. The PTC accounts for 71% of the total investment cost, mainly due to the large number of PTCs incorporated into the MGS. The ORC subsystem follows with 13.2%, indicating that, while smaller, it still substantially contributes to the required capital expenditure, primarily due to the large number of components. The RO subsystem represents about 7% of the total cost, while the ARC subsystem represents 6.5%, both showing moderate cost shares in the system. In addition, TES contributes for 1. 7%, while PEME contributes only 0.36% of the total cost, mainly because its low capacity resulting from the preliminary design aimed at meeting the required demand for hydrogen production. Overall, the figure emphasizes the dominance of the PTC subsystem in determining the overall investment cost due to the high number of parallel PTC used in the MGS.

Fig. 10 presents a comparison of economic parameters for three different configurations: the ORC+PTC+TES system, the MGS system with and without TES. The results show that the complete MGS system (with TES) performs best economically, with an NPV of $8.08 million, a PP of 3.8 years, and an IRR of 30%. In comparison, the MGS system without TES achieves an NPV of $6.4 million, a PP of 4.8 years, and an IRR of 21%, still performing better than the ORC+PTC+TES system, which exhibits values of $3 million, 7.3 years, and 17% for NPV, PP, and IRR, respectively.

The economic advantage of the MGS system (with or without TES) is attributed to its modular design, which reduces operational and maintenance costs while enabling the simultaneous generation of multiple energy products. Furthermore, the integration of TES in the complete MGS system enhances economic indicators by allowing for more efficient utilization of stored thermal energy and reducing energy losses.

Although the incorporation of the TES unit increases the initial capital cost, this increase is offset by the reduction in the required capacity of the PTC and other system components. Consequently, the

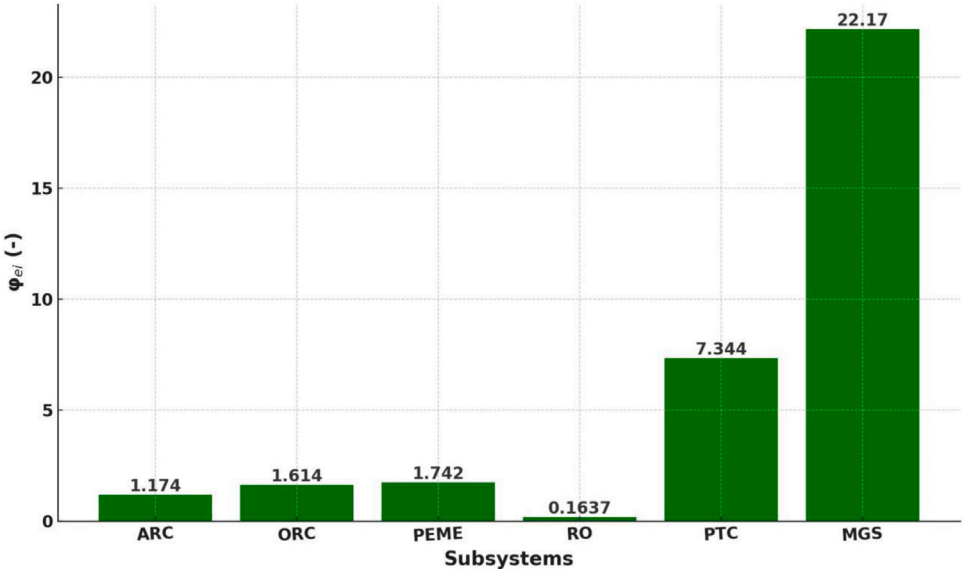

Fig. 7. Environmental damage effectiveness (EDE) factor for each subsystem and MGS.

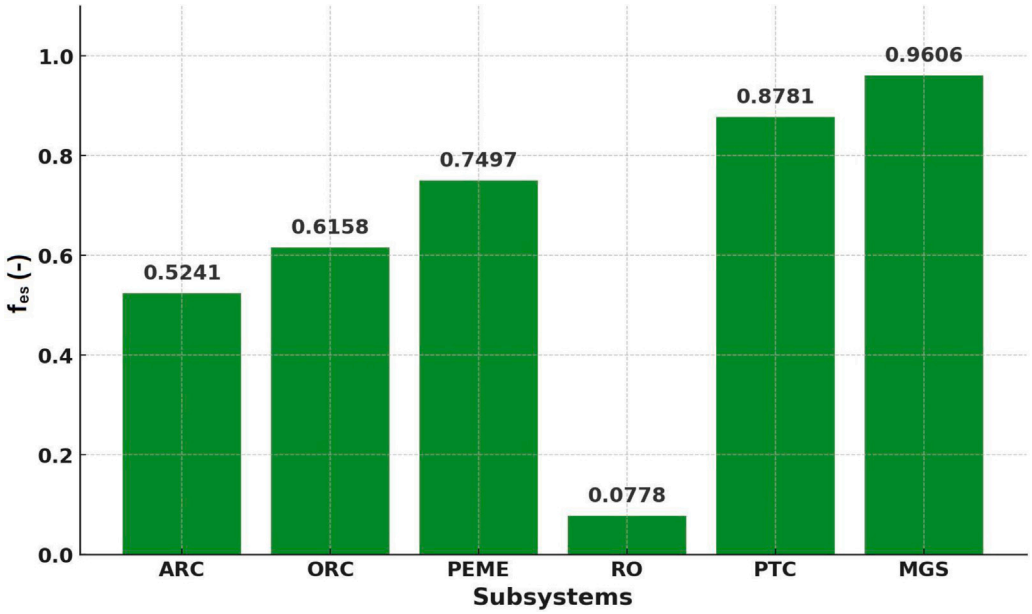

Fig. 8. Exergy stability factor (ESF) factor for each subsystem and MGS.

inclusion of TES proves to be economically viable and contributes to the overall optimization of the system design.

In contrast, the ORC+PTC+TES system suffers from lower profitability and slower investment returns due to its single-purpose energy conversion and higher dependence on thermal storage, making it more appropriate for long-term, low-risk investments but less attractive in terms of economic performance.

3.5. Sensitive analysis results

Fig. 11a shows the effect of changes in the size of the TES, PTC, and ORC systems on PP (payback period) and NPV (net present value). Increasing the mass flow rate of the working fluid in the ORC increases the electricity produced and, consequently, the size of the PTC and TES systems. It can be observed that these changes have a positive effect on the economic parameters of the system; the PP of ORC + PTC + TES as well as of the MGS decreases, indicating a reduction of the risk associated with the investment. In parallel, NPV increases in both cases, indicating a better profitability of the project over its operating life.

Fig. 11b shows the effect of changing the size of the TES, PTC, and ORC systems on the energy and exergy efficiencies of the MGS. Unlike the economic parameters, changing the size of the ORC + PTC + TES systems does not have a significant effect on the energy and exergy efficiencies of the MGS, indicating the stability of the efficiency of this system concerning changes in the size of its components.

On the other hand, increasing the mass flow rate of point 10, which increases the mass flow rate in the entire ORC and its size, and consequently, in the PTC, two opposing effects are observed: (i) it increases the electricity produced by the ORC, and consequently, the energy and exergy efficiencies of the MGS increase (positive effect); (b) it causes the increase of heat losses from the ORC exchangers and in the PTC (negative effect). Up to a mass flow rate of 3.5 kg/s, the first effect dominates on the second oner, and as a result, the energy and exergy efficiencies of the MGS increase. At a mass flow rate of 4 kg/s,

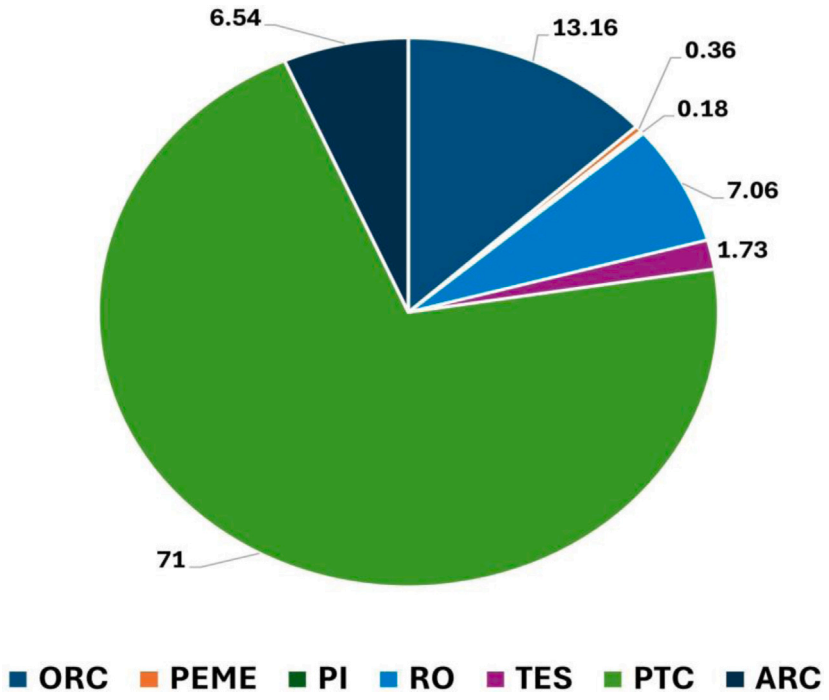

Fig. 9. Cost distribution of each subsystem as a percentage of the total cost.

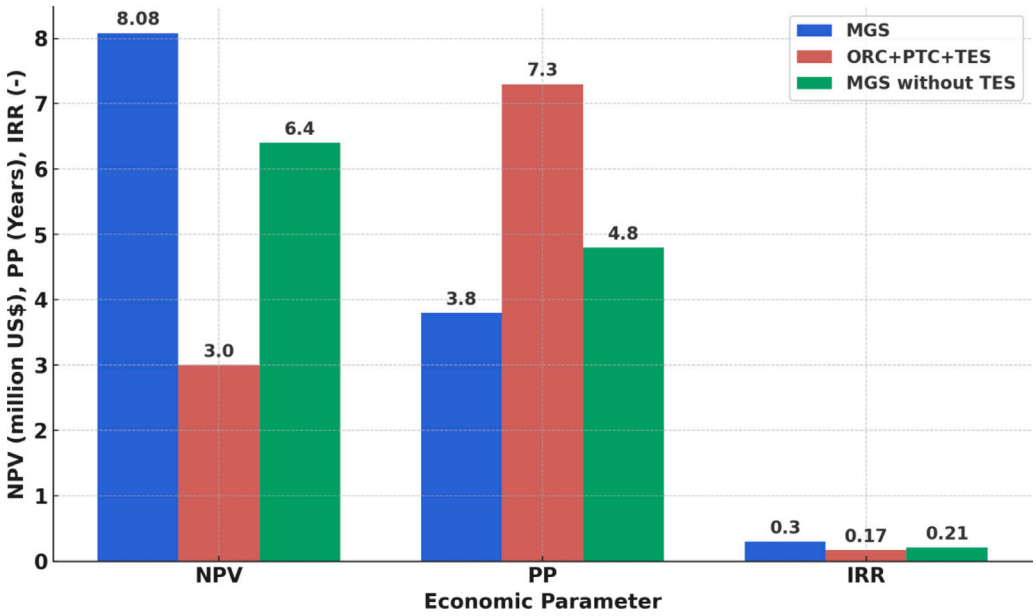

Fig. 10. Economic parameters for ORC+PTC+TES,MGS with and without TES.

the second effect dominates, leading to a decrease in energy and exergy efficiencies.

The highest energy efficiency value (12.2%) is obtained at a mass flow rate of 3.5 kg/s. This value indicates that at this point, the MGS system has an optimal performance in terms of energy efficiency. On the other hand, the highest exergy efficiency value (4.38%) is observed at a mass flow rate of 5.5 kg/s. These results show that, unlike economic parameters that have an increasing trend, energy and exergy efficiency have a more fluctuating behaviour and are not significantly affected by the size of each subsystems. Therefore, the optimization of the performance of the MGS system in terms of efficiency, and other influential parameters such as operating conditions and inlet temperature should be preferred instead of changing the size of ORC, PTC, and TES.

Fig. 11c shows the variation of the environmental factors (i.e., exergo-environmental, environmental damage effectiveness, and exergy stability factors) with the increase in the mass flow rate of the working fluid in the ORC. As mentioned before, the minimum value of these environmental factors is considered as the optimal condition, since their decrease indicates a reduction of environmental impacts and an increase in the efficiency of the system in terms of exergy stability and environmental impacts. The results obtained indicate that similar to the energy and exergy efficiencies, the changes in these

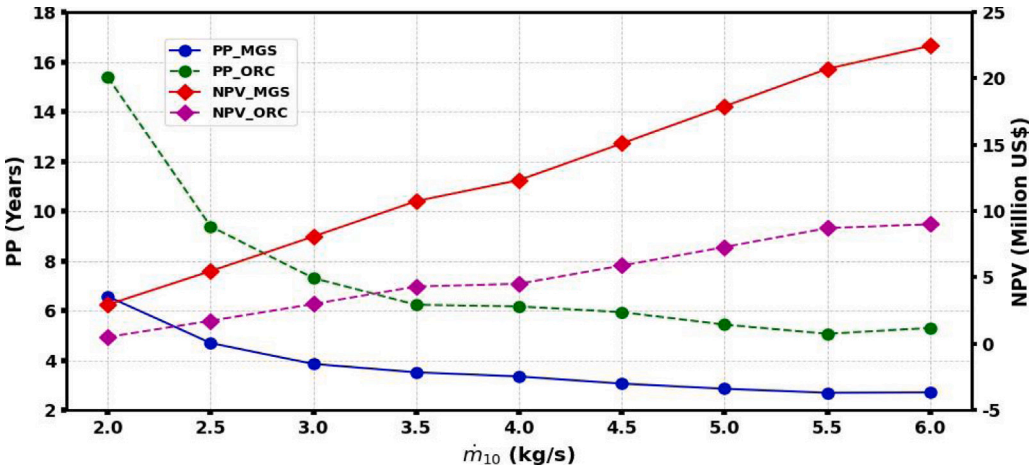

(a) PP and NPV parameters

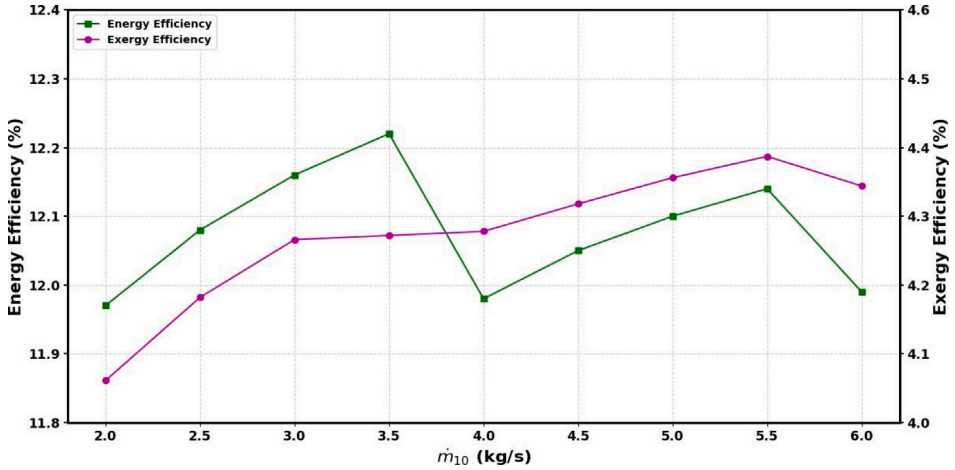

(b) Energy and exergy efficiencies

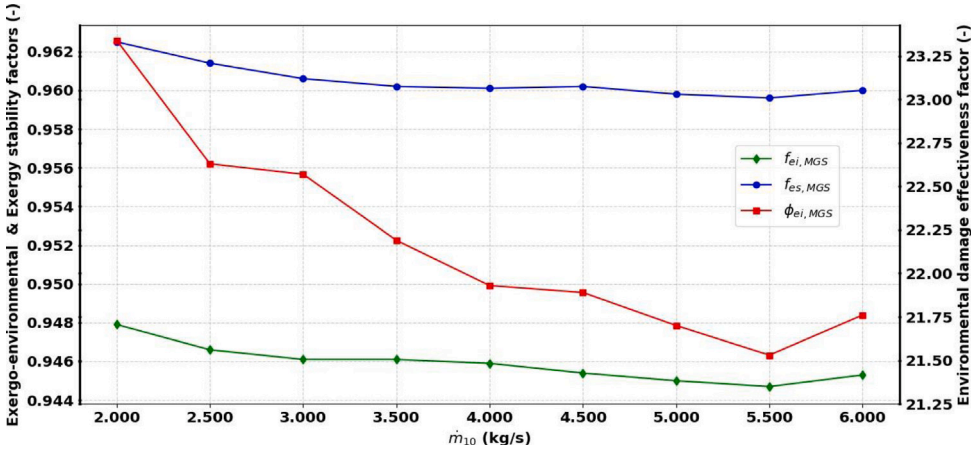

(c) Exergo-environmental, environmental damage effectiveness, and exergy stability factors

Fig. 11. Economic, energy, and exergy efficiencies, and environmental parameters versus ORC mass flow rate.

environmental factors are also not significant. In other words, the increase in the mass flow rate of the working fluid in the ORC does not significantly improve the system's environmental performance and the changes in these parameters remain within a limited range.

Fig. 12a depicts the variation of the NPV and PP with the PEME power consumption, assuming the 2025 product price as reference, to provide an up-to-date analysis of the economic performance of the system. The results obtained shows that increasing the PEME power consumption, which leads to an increase in the hydrogen production, is not economically desirable. Since this increase causes almost quasi-linear changes in the economic parameters, it will either lead to an increase in the pay-back period and/or a decrease in NPV. Therefore,

under the current conditions, increasing the PEME power consumption harms the economic performance of the system. However, technological developments resulting in a more efficient PEME system might lead to significant changes and more favourable economic conditions of this subsystem. Therefore, improving the efficiency of PEME and deploying innovative and more effective energy management techniques can play a key role in improving the economic efficiency of this system.

Fig. 12b shows the correlation between the energy and exergy efficiencies of the MGS and the power consumption of the PEME. The analysis focuses on how the MGS efficiencies change when all of the electricity generated is used for hydrogen production in the electrolyzer. The results indicate that as the power consumed by the PEME increases, the MGS energy and exergy efficiencies decrease in a quasi-linear pattern, mainly due to a significant portion of the electricity consumed by the PEME, where significant energy losses, such as heat dissipation and resistive losses, occur. Similarly, the exergy efficiency decreases since the hydrogen production process involves irreversible transformations, including entropy generation and the conversion of high-quality electrical energy into chemical energy.

Fig. 12c illustrates the changes of the environmental factors (namely, the exergo-environmental factor, the effectiveness of environmental damage, and the stability of exergy) with the power consumption of PEME. As the power consumption of PEME increases, the amount of hydrogen produced by the system also increases. This increment leads to an almost linear growth of all three environmental factors with the increased power consumption of the electrolyzer. From an environmental point of view, this trend is considered undesirable since it indicates an increase of negative environmental impacts, directly related to the augmented electricity consumption in PEME.

Therefore, it can be concluded that using part of the electricity produced by ORC in the PEME for hydrogen production is not a suitable solution in terms of reducing the environmental impacts of the system. This shows that although hydrogen production is a sustainable and suitable route for energy storage, in these specific conditions, increasing its production and, consequently, the associated electric consumption, will increase the negative environmental impacts of the system. Therefore, optimizing and increasing the environmental performance of the system requires strategies to reduce PEME power consumption or improve energy conversion efficiency in ORC and PEME.

Finally, Fig. 13 illustrates the variations in the energy and exergy efficiencies of the MGS as a function of the solar radiation. As observed in the figure, an increase in solar radiation leads to a slight increase in the energy and exergy efficiencies of the system. This behaviour can be attributed to the complex relationship between solar energy utilization and the associated losses within the MGS. As solar radiation increases, the MGS absorbs more energy, which theoretically provides a higher potential for useful energy conversion. This increase in input energy enhances the ability of the MGS to generate electricity, heat, or other outputs, contributing positively to energy and exergy efficiencies. However, the increased solar input also leads to higher radiative and thermal losses, which act as a counterbalance to the increased energy input, thereby limiting the extent to which the efficiencies improve.

4. Conclusions

This study presents a comprehensive 4E assessment that includes energy, exergy, economic, and exergo-environmental analyses of a solar-powered multigeneration solar (MGS). The system integrates parabolic trough collectors (PTCs), thermal energy storage (TES), organic Rankine cycle (ORC), absorption refrigeration cycle (ARC), and proton exchange membrane electrolyzer (PEME) to simultaneously generate electricity, PW, cooling, and hydrogen. The multifunctionality of the solar-powered multigeneration system (MGS) presents both opportunities and challenges. On one hand, the generation of diverse products – including electricity, potable water (PW), cooling, and hydrogen – improves resource utilization and system versatility. This is particularly valuable in meeting energy and water demands in arid and isolated regions. However, the various subsystems increase the system's thermodynamic irreversibilities.

The overall energy and exergy efficiencies of the MGS were calculated as 12.2% and 4.38%, respectively. These values confirm the moderate thermodynamic performance of multigeneration systems due to their complex structure and energy distribution among multiple outputs.

From an economic point of view, the MGS achieved a net present value (NPV) of nearly $8 million and a payback period of 3.8 years, confirming its strong investment potential in solar-rich regions. The large cost share of parabolic trough collectors (PTCs) shows the need for advanced solar collection technologies that can maximize energy capture with fewer collectors to reduce initial investment costs. In addition, the integration of TES enables continuous operation and improves the economic viability of a solar-powered multigeneration system (MGS). This highlights the importance of energy storage in renewable energy systems, as it allows a better matching of energy supply with demand.

The exergo-environmental analysis highlights the importance of considering the environmental impact of energy systems with their thermodynamic performance. Exergy destruction rate (EDR) is directly related to resource depletion and environmental damage. Reducing the exergy destruction rate (EDR) in the main subsystems, such as PTC and ORC, is essential to improve the sustainability of the system. Strategies such as enhanced heat recovery, reduced pressure losses, and optimized flow configurations can significantly reduce exergy destruction rate (EDR).

The PTC subsystem accounts for the highest EDE value of 7.344 and the overall MGS has the maximum EDE of 22.17, showing the critical importance of minimizing irreversibilities in solar thermal energy conversion. In contrast, the RO subsystem, with an exergo-environmental factor of only 0.0419, shows the lowest environmental burden.

The parametric analyses show the critical role of solar radiation in solar-powered multigeneration system (MGS) economic parameters such as payback period (PP) due to the reduction size of the MGS. However, it has a lesser effect on the energy and exergy efficiencies of the multigeneration system (MGS), since the higher solar radiation causes higher radiative and thermal losses. These losses reduce solar-powered multigeneration system (MGS) performance from the energy and exergy perspective. These findings emphasize the need for location-specific designs and operational strategies that maximize the benefits of solar resources while minimizing losses.

Moreover, sensitivity analysis shows that increasing the ORC mass flow rate to 3.5 kg/s maximizes the energy efficiency of the system, whereas exergy efficiency peaks at a flow rate of 5.5 kg/s. These insights can be leveraged to fine-tune the component sizing and improve system-level performance.

Scalability is a fundamental aspect in the operational implementation of the proposed solar multigeneration system (MGS). The modular nature of the system allows for high adaptability to different applications, such that it can be expanded from small and decentralized scales to larger scales at the district or town level. This flexibility ensures that the system is able to meet the energy needs of different populations without the need for major redesign.

From a geographical and climatic perspective, the system has the greatest potential in areas with high solar radiation, especially arid and semi-arid regions, where both electricity and fresh water are in high demand. In coastal or humid areas, the integration of desalination technologies within the multigeneration system provides significant added value. However, in cold climates or areas with long periods of low radiation, the system performance may be reduced unless supported by auxiliary heat sources or thermal storage systems.

Despite its modular structure, scaling up this system presents its own technical and economic challenges. These include the need for more land to install solar collectors, increased initial investment costs,

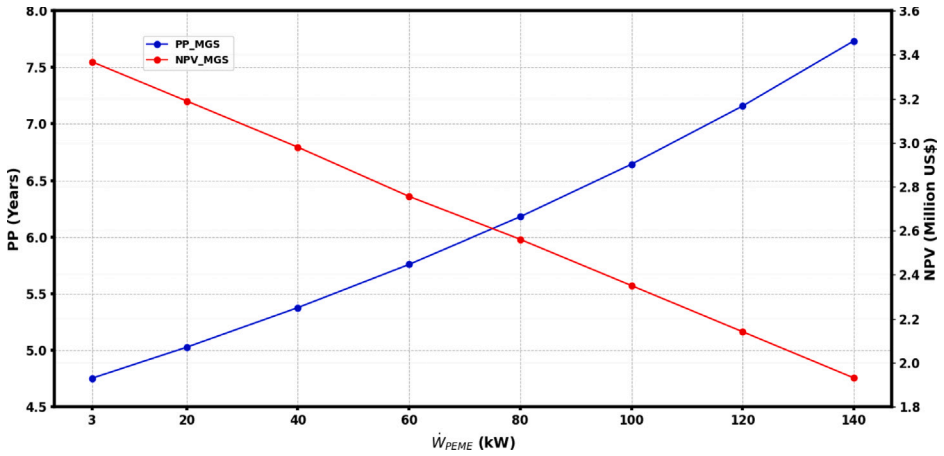

(a) PP and NPV parameters

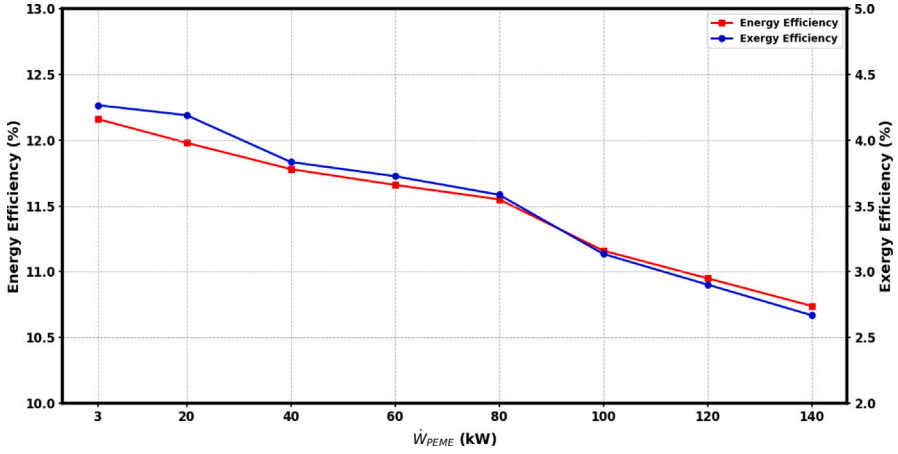

(b) Energy and exergy efficiencies

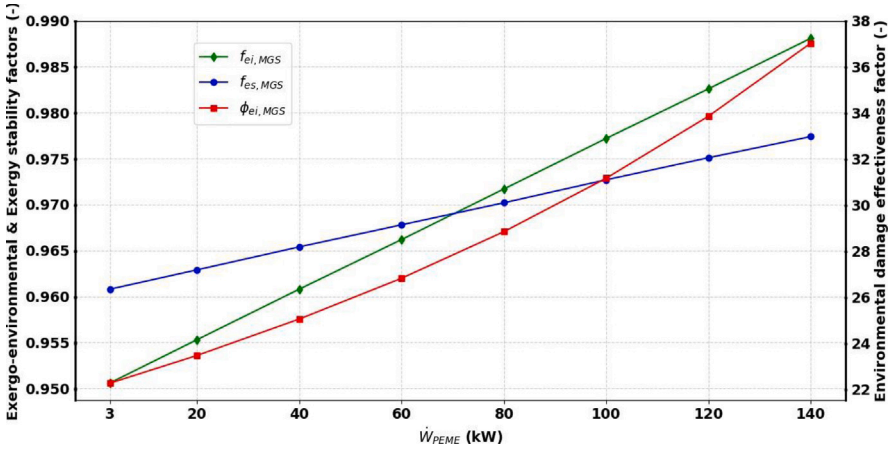

(c) Exergo-environmental, environmental damage effectiveness, and exergy stability factors

Fig. 12. Economic, energy, and exergy efficiencies, and environmental parameters versus PEME power consumption.

and increased complexity in control strategies for operating the system, especially when multiple energy carriers such as hydrogen or electrical storage are combined. Furthermore, careful planning and possibly structural modifications will be required for effective integration with existing energy infrastructure, depending on local grid architecture and regulations.

Since this study provides a preliminary design and performance evaluation of the multigeneration system future research activities should perform a comprehensive investigation of its scalability under diverse environmental and infrastructure conditions.

It is important to acknowledge that the implementation of real-time control strategies can significantly affect system performance.

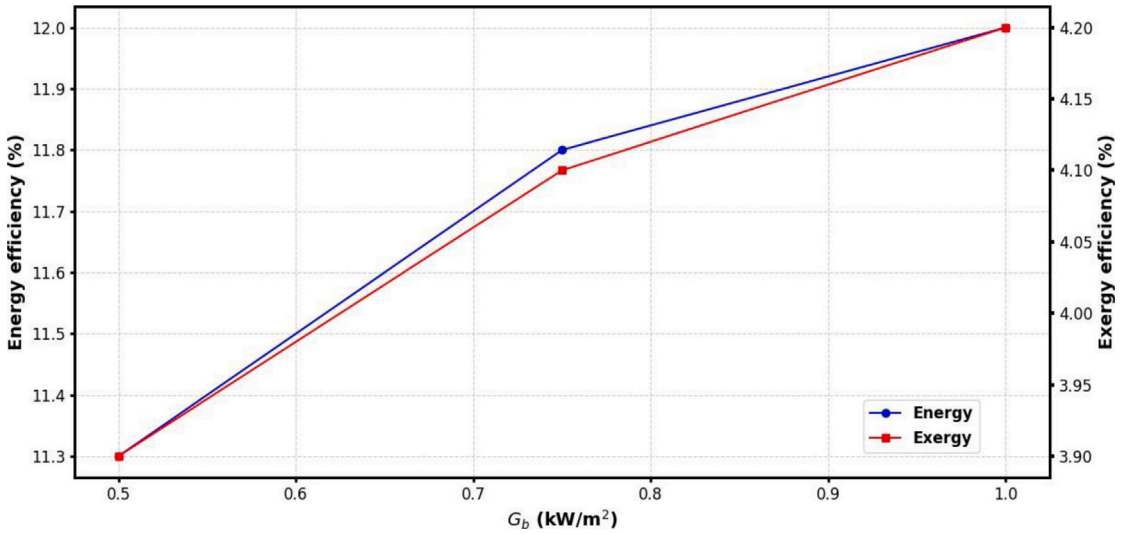

Fig. 13. Energy and exergy efficiencies of the MGS versus solar radiation.

Advanced control techniques—such as model predictive control (MPC), or adaptive regulation can adjust mass flow rates, component set-points, and subsystem interactions to reduce irreversibilities and enhance energy management under variable solar and load conditions. Such control strategies are especially relevant in systems like MGS, where thermal and electrical subsystems are tightly coupled and operate under fluctuating boundary conditions. However, the design and validation of control strategies require detailed controller tuning and real-time data acquisition frameworks, which are beyond the scope of the current work. Nevertheless, the component-level exergy and energy mappings provided in this study form a solid foundation for future dynamic modelling and control-oriented optimization of multigeneration systems.

Nomenclature

Abbreviations

- **ARC**: Absorption Refrigeration Cycle
- **CAES**: Compressed Air Energy Storage
- **COP**: Coefficient of Performance
- **EDE**: Environmental Damage Effectiveness
- **ENE**: Energy Efficiency
- **EDR**: Exergy Destruction Rate
- **ERC**: Ejector Refrigeration Cycle
- **ESF**: Exergy Stability factor
- **EXE**: Exergy Efficiency
- **HX**: Heat Exchanger
- **IRR**: Internal Rate of Return
- **LCOE**: Levelized Cost of Electricity
- **MED**: Multi-Effect Distillation
- **MGS**: Multi-Generation System
- **NPV**: Net Present Value
- **ORC**: Organic Rankine Cycle
- **PCM**: Phase Change Material
- **PEME**: Proton Exchange Membrane Electrolyzer
- **PP**: Payback Period
- **PTC**: Parabolic Trough Collector
- **RO**: Reverse Osmosis
- **SOFC**: Solid Oxide Fuel Cell
- **TES**: Thermal Energy Storage
- **TEG**: Thermoelectric Generato

Symbols

- A: General area (m^2)
- A_{ap}: Aperture area of the collector (m^2)
- A_{re}: Receiver area (m^2)
- A_c: Cover area (m^2)
- C: Cost (US$)
- C_F: Annual cash flow (US$)
- C_n: Total investment cost (US$)
- C_0: Initial investment cost (US$)
- c: Specific heat capacity (J/kg K)
- c_{HTF}: Specific heat of Heat Transfer Fluid (J/kg K)
- D_2: Inner diameter of the absorber (m)
- D_3: Outer diameter of the absorber (m)
- D_4: Inner diameter of the glass envelope (m)
- D_5: Outer diameter of the glass envelope (m)
- D_{oc}: Outer cover diameter (m)
- E_{ES}: Thermal energy stored in charge mode (kWh or J)
- E_{RES}: Thermal energy required for discharge mode (kWh or J)
- ΔE: Change in energy (J or kJ)
- F: Faraday constant (96,485 C/mol)
- f_{ei}: Exergoenvironmental factor (–)
- f_{es}: Exergy stability factor (–)
- F_R: Heat removal factor (–)
- F_1: Collector efficiency factor (–)
- ΔG: Gibbs free energy (kJ/mol)
- G_b: Solar radiation (W/m^2)
- g: Gravitational acceleration (9.81 m/s^2)
- h: Specific enthalpy (J/kg)
- h_{cca}: Convective heat transfer coefficient (W/m^2 K)
- h_{rca}: Radiative heat transfer coefficient (W/m^2 K)
- h_{rcr}: Radiation heat transfer coefficient between receiver and cover (W/m^2 K)
- i: Discount rate or interest rate (–)
- IRR: Internal Rate of Return (–)
- J: Current density (A/m^2)
- $J_{0,i}$: Exchange current density (A/m^2)
- K:
  - Specific cost per unit of the product (US$/unit)
  - Investment cost of subsystems (US$)
- K_γ: Incidence angle modifier (–)

- L: Collector length (m) or membrane thickness (m)
- m: General mass (kg)
- $\dot{m}$: Mass flow rate (kg/s)
- $\dot{m}_{oil}$: Thermal oil mass flow rate (kg/s)
- $\dot{m}_{re}$: Receiver mass flow rate (kg/s)
- $\dot{N}_{\mathrm{H_2.out}}$: Rate of hydrogen generation during electrolysis (mol/s)
- $\dot{N}_{\mathrm{H_2O.reacted}}$: Rate of water consumed during electrolysis (mol/s)
- N: Number of periods (e.g., years) or total number of rows
- N_{PTC}: Number of parabolic trough collectors (–)
- NPV: Net Present Value (US$)
- Nu_{ca}: Nusselt number of convective air (–)
- P: Pressure (kPa)
- PP: Payback Period (years)
- Pr_a: Prandtl number of air (–)
- Pr_c: Prandtl number of cover (–)
- Q: Heat transfer rate (kW)
- $\dot{Q}_u$: Usable energy rate (kW)
- Q_{ch}: Heat stored during charging (kJ)
- Q_{cd}: Heat released during discharging (kJ)
- $Q_{\mathrm{in\text{-}TES}}$: Heat input to the TES (kJ)
- $Q_{\mathrm{loss,ch}}$: Heat loss during charging (kJ)
- $Q_{\mathrm{loss,cd}}$: Heat loss during discharging (kJ)
- r: Discount factor (e.g., 3
- RR: Recovery Ratio (–)
- R: Universal gas constant (8.314 J/mol K)
- Re_{ca}: Reynolds number for convective air (–)
- S:
  - Solar radiation absorbed (W/m^2)
  - Entropy (kJ/K mol)
- t_c: Duration of charging (s or h)
- t_d: Duration of discharging (s or h)
- T_{ch}: Charging tank temperature (K)
- T_{cd}: Cold tank discharge temperature (K)
- T_{dh}: Hot tank discharge temperature (K)
- T_{dd}: Cold tank discharging temperature (K)
- T_a: Ambient temperature (K)
- T_c: Cover temperature (K)
- T_{ic}: Initial temperature of the charging process (K)
- T_{id}: Initial temperature of the discharging process (K)
- T_r: Receiver temperature (K)
- $T_{\max}$: Maximum temperature of thermal oil (K)
- $T_{\min}$: Minimum temperature of thermal oil (K)
- U_L: Overall heat loss coefficient (W/m^2 K)
- U_{ar}: Absorber–receiver heat transfer coefficient (W/m^2 K)
- V: Velocity (m/s) or Volume (m^3) (context-dependent)
- V_{tank}: Tank volume (m^3)
- W: Work or power output (kW or kJ)
- $\dot{W}$: Power or work rate (kW)
- $\dot{W}_{\mathrm{net}}$: Net power output (kW)
- $\dot{W}_{P,\mathrm{RO}}$: Work required for RO pump (kW)
- $\dot{W}_{\mathrm{expander}}$: Work output of the expander (kW)
- x:
  - Membrane depth (m)
  - Concentration of salt (–)
- Y: Production per year (units/year)
- z: Height (m)

Greek symbols

- α: Absorptance of the receiver (–)
- ϵ: Emissivity (–)
- η: Efficiency (–)
- η_r: Solar collector efficiency (–)
- $\lambda(x)$: Local water content in the membrane at depth x (–)
- η_{en}: Energy efficiency (–)
- η_{ex}: Exergy efficiency (–)
- η_{HX}: Heat exchanger effectiveness (–)
- $\eta_{\mathrm{act.a}}$: Anode activation overpotential (V)
- $\eta_{\mathrm{act.c}}$: Cathode activation overpotential (V)
- η_{ohm}: Ohmic overpotential (V)
- γ: Intercept factor (–)
- $\lambda(x)$: Local water content in the membrane (–)
- π: Osmotic pressure (Pa)
- ρ: Density (kg/m^3)
- σ: Stefan–Boltzmann constant (W/m^2 K^4)
- τ: Transmittance of the cover (–)
- Ψ: Specific exergy (kJ/kg)
- Δ: Change or difference between two values (–)

Subscripts

- ap: Aperture
- ar: Absorber–receiver
- c: Collector or cover
- ch: Charging
- cd: Cold discharge
- d: Discharge
- dd: Discharging mode, cold storage tank
- dh: Discharging mode, hot storage tank
- en: Energy-related term
- ex:
  - Expander
  - Exergy-related term
- an: Anode
- ca: Cathode
- E: Evaporator
- G: Generator
- htf: Heat Transfer Fluid
- hx: Heat exchanger
- i: Inlet or initial
- o: Outlet
- re: Receiver
- r: Receiver or reflectance
- SW: Seawater
- PW: Potable water
- BW: Brine water
- oil: Thermal oil
- $tank$: Storage tank

CRediT authorship contribution statement

Mattia De Rosa: Conceptualization, Writing – review & editing, Writing – original draft, Validation, Methodology, Funding acquisition, Formal analysis. **Mehdi Aliehyaei:** Writing – review & editing, Writing – original draft, Validation, Methodology, Formal analysis, Conceptualization.

Declaration of competing interest

The authors declare the following financial interests/personal relationships which may be considered as potential competing interests: Mattia De Rosa reports financial support was provided by European Commission. If there are other authors, they declare that they have no known competing financial interests or personal relationships that could have appeared to influence the work reported in this paper.

Acknowledgements

The present research was funded by the European Union in the framework of the EU LIFE project RESSKILL (Grant n. 101167278). Views and opinions expressed are however those of the authors only and do not necessarily reflect those of the European Union or the granting authority. Neither the European Union nor the granting authority can be held responsible for them.

Data availability

Data will be made available on request.

References

[1] S. Sadeghi, S. Ghandehariun, B. Rezaie, Energy and exergy analyses of a solar-based multi-generation energy plant integrated with heat recovery and thermal energy storage systems, Appl. Therm. Eng. 188 (2021) 116629.
[2] A. Bozgeyik, L. Altay, A. Hepbasli, A sub-system design comparison of renewable energy based multi-generation systems: A key review along with illustrative energetic and exergetic analyses of a geothermal energy based system, Sustain. Cities Soc. 82 (2022) 103893.
[3] N. Azizi, F. Esmaeilion, S.F. Moosavian, M. Yaghoubirad, A. Ahmadi, M. Aliehyaei, M. Soltani, Critical review of multigeneration system powered by geothermal energy resource from the energy, exergy, and economic point of views, Energy Sci. Eng. 10 (12) (2022) 4859–4889.
[4] J. Ahmed, L. Kumar, A.F. Abbasi, M. El Haj Assad, Energy, exergy, environmental and economic analysis (4e) of a solar thermal system for process heating in jamshoro, Pakistan, Energies 15 (22) (2022).
[5] X. Zhou, C. Ding, A.M. Abed, S. Abdullaev, S.F. Ahmad, Y. Fouad, M. Dahari, I. Mahariq, Techno-economic assessment and transient modeling of a solar-based multi-generation system for sustainable/clean coastal urban development, Renew. Energy 233 (2024) 121119.
[6] C. Zhu, M. Wang, M. Guo, J. Deng, Q. Du, W. Wei, Y. Zhang, S.S. Ashraf Talesh, Optimizing solar-driven multi-generation systems: A cascade heat recovery approach for power, cooling, and freshwater production, Appl. Therm. Eng. 240 (2024) 122214.
[7] K. Mohammadi, S. Khanmohammadi, H. Khorasanizadeh, K. Powell, A comprehensive review of solar only and hybrid solar driven multigeneration systems: Classifications, benefits, design and prospective, Appl. Energy 268 (2020) 114940.
[8] J. Fang, M. Yang, Y. Fan, T. Luo, H. Li, T. Liu, S. Tang, K. Zhao, Thermodynamic evaluation of a combined cooling, heating, hydrogen, and power multi-generation system for full-spectrum solar energy utilization, Energy Convers. Manage. 300 (2024) 118019.
[9] M.J. Shabani, M. Babaelahi, Innovative solar-based multi-generation system for sustainable power generation, desalination, hydrogen production, and refrigeration in a novel configuration, Int. J. Hydrog. Energy 59 (2024) 1115–1131.
[10] S. Ozlu, I. Dincer, Performance assessment of a new solar energy-based multigeneration system, Energy 112 (2016) 164–178.
[11] O. Bamisile, Q. Huang, W. Hu, M. Dagbasi, A.D. Kemena, Performance analysis of a novel solar PTC integrated system for multi-generation with hydrogen production, Int. J. Hydrog. Energy 45 (1) (2020) 190–206.
[12] N. Zheng, H. Zhang, L. Duan, Q. Wang, A. Bischi, U. Desideri, Techno-economic analysis of a novel solar-driven PEMEC-SOFC-based multi-generation system coupled parabolic trough photovoltaic thermal collector and thermal energy storage, Appl. Energy 331 (2023) 120400.
[13] P. Pourmoghadam, A. Kasaeian, Economic and energy evaluation of a solar multi-generation system powered by the parabolic trough collectors, Energy 262 (2023) 125362.
[14] V.K. Chauhan, S.K. Shukla, J.V. Tirkey, P.K.S. Rathore, A comprehensive review of direct solar desalination techniques and its advancements, J. Clean. Prod. 284 (2021) 124719.
[15] Ş. Kılkış, G. Krajačić, N. Duić, M.A. Rosen, et al., Effective mitigation of climate change with sustainable development of energy, water and environment systems, 269, 2022, 116146,
[16] S. Khaleghi, S. Asiaei, M. Siavashi, A smart grid poly-generation design for hot arid regions composed of multi-effect distillation (MED), compressed air energy storage (CAES), and parabolic trough solar collector field (PTSC), J. Clean. Prod. 372 (2022) 133693.
[17] F.A. Al-Sulaiman, F. Hamdullahpur, I. Dincer, Performance assessment of a novel system using parabolic trough solar collectors for combined cooling, heating, and power production, Renew. Energy 48 (2012) 161–172.
[18] D.G. Hurst, Engineering heat transfer, Nucl. Sci. Eng. 18 (1964) 539–540.
[19] S. Toghyani, E. Baniasadi, E. Afshari, Thermodynamic analysis and optimization of an integrated rankine power cycle and nano-fluid based parabolic trough solar collector, Energy Convers. Manage. 121 (2016) 93–104.
[20] S.C. Kaushik, S. Kumar, Finite time thermodynamic evaluation of irreversible ericsson and stirling heat engines, Energy Convers. Manage. 42 (2001) 295–312.
[21] M.F. Qureshi, M.W. Chandio, A.A. Memon, L. Kumar, M.M. Awad, Thermal analysis of solar energy based organic rankine cycle cascaded with vapor compression refrigeration cycle, Energy Nexus 14 (2024) 100291.
[22] R. Yargholi, H. Kariman, S. Hoseinzadeh, M. Bidi, A. Naseri, Modeling and advanced exergy analysis of integrated reverse osmosis desalination with geothermal energy, Water Supply 20 (3) (2020) 984–996.
[23] A. Naseri, M. Bidi, M.H. Ahmadi, Thermodynamic and exergy analysis of a hydrogen and permeate water production process by a solar-driven transcritical CO_2 power cycle with liquefied natural gas heat sink, Renew. Energy 113 (2017) 1215–1228.
[24] H.T. El-Dessouky, H.M. Ettouney, Chapter 7 - reverse osmosis, in: Fundamentals of Salt Water Desalination, Elsevier Science B.V., 2002, pp. 409–437.
[25] H.T. El-Dessouky, H.M. Ettouney, Chapter 8 - reverse osmosis feed treatment, biofouling, and membrane cleaning, in: Fundamentals of Salt Water Desalination, Elsevier Science B.V., 2002, pp. 439–452.
[26] G. Tchobanoglous, F.L. Burton, H.D. Stensel, Wastewater Engineering: Treatment and Reuse, fourth ed., McGraw-Hill, 2003.
[27] L. Malaeb, G.M. Ayoub, Reverse osmosis technology for water treatment: State of the art review, Desalination 267 (1) (2011) 1–8.
[28] I. Metcalf & Eddy, Water Reuse: Issues, Technologies, and Applications, McGraw-Hill, 2014.
[29] M. Ni, M.K. Leung, D.Y.C. Leung, Energy and exergy analysis of hydrogen production by solid oxide steam electrolyzer plant, Int. J. Hydrog. Energy 32 (18) (2007) 4648–4660, Cited by: 211.
[30] M. Ni, M.K.H. Leung, D.Y.C. Leung, Energy and exergy analysis of hydrogen production by a proton exchange membrane (PEM) electrolyzer plant, Energy Convers. Manage. 49 (10) (2008) 2748–2756.
[31] A.H. Keshavarzzadeh, P. Ahmadi, Multi-objective techno-economic optimization of a solar-based integrated energy system using various optimization methods, Energy Convers. Manage. 196 (2019) 196–210.
[32] M.A. Ehyaei, A. Ahmadi, M. El Haj Assad, M.A. Rosen, Investigation of an integrated system combining an organic rankine cycle and absorption chiller driven by geothermal energy: Energy, exergy, and economic analyses and optimization, J. Clean. Prod. 258 (2020) 120780.
[33] A. Lazzaretto, G. Tsatsaronis, SPECO: A systematic and general methodology for calculating efficiencies and costs in thermal systems, Energy 31 (2006) 1257–1289.
[34] A. Bejan, G. Tsatsaronis, M. Moran, Thermal Design and Optimization, John Wiley and Sons, Inc., 1996.
[35] T.A.H. Ratlamwala, I. Dincer, M.A. Gadalla, Comparative environmental impact and sustainability assessments of hydrogen and cooling production systems, Causes, Impacts Solutions To Glob. Warm. (2013) 389–408.
[36] T.A.H. Ratlamwala, I. Dincer, B.V. Reddy, Exergetic and environmental impact assessment of an integrated system for utilization of excess power from thermal power plant, Causes, Impacts Solutions To Glob. Warm. (2013) 803–824.
[37] A. Midilli, I. Dincer, Development of some exergetic parameters for PEM fuel cells for measuring environmental impact and sustainability, Int. J. Hydrog. Energy 34 (9) (2009) 3858–3872.
[38] E. Bellos, S. Pavlovic, V. Stefanovic, C. Tzivanidis, B.B. Nakomcic-Smaradgakis, Parametric analysis and yearly performance of a trigeneration system driven by solar-dish collectors, Int. J. Energy Res. 43 (4) (2019) 1534–1546.
[39] C. Tzivanidis, E. Bellos, K.A. Antonopoulos, Energetic and financial investigation of a stand-alone solar-thermal organic rankine cycle power plant, Energy Convers. Manage. 126 (2016) 421–433.
[40] S.A. Makkeh, A. Ahmadi, F. Esmaeilion, M.A. Ehyaei, Energy, exergy and exergoeconomic optimization of a cogeneration system integrated with parabolic trough collector-wind turbine with desalination, J. Clean. Prod. 273 (2020) 123122.
[41] R. Shirmohammadi, A. Aslani, R. Ghasempour, L.M. Romeo, F. Petrakopoulou, Techno-economic assessment and optimization of a solar-assisted industrial post-combustion CO2 capture and utilization plant, Energy Rep. 7 (2021) 7390–7404.
[42] A. Ahmadi, D.H. Jamali, M.A. Ehyaei, M.E.H. Assad, Energy, exergy, economic and exergoenvironmental analyses of gas and air bottoming cycles for production of electricity and hydrogen with gas reformer, J. Clean. Prod. 259 (2020) 120915.
[43] H. Nami, E. Akrami, Analysis of a gas turbine based hybrid system by utilizing energy, exergy and exergoeconomic methodologies for steam, power and hydrogen production, Energy Convers. Manage. 143 (2017) 326–337.
[44] R. Shirmohammadi, A. Aslani, R. Ghasempour, L.M. Romeo, F. Petrakopoulou, Process design and thermoeconomic evaluation of a CO2 liquefaction process driven by waste exhaust heat recovery for an industrial CO2 capture and utilization plant, J. Therm. Anal. Calorim. 145 (3) (2021) 1585–1597.
[45] Eurostat, Electricity price statistics, 2024, (Accessed March 2024), https://ec.europa.eu/eurostat/statistics-explained/index.php/Electricity_price_statistics.

[46] Water News Europe, Water prices compared in 36 EU cities, 2024, (Accessed March 2024), https://www.waternewseurope.com/water-prices-compared-in-36-eu-cities/.
[47] Water News Europe, Water prices compared in 36 EU-cities, 2021, (Accessed 03 February 2025).
[48] International Renewable Energy Agency (IRENA), Green hydrogen cost reduction: Scaling up electrolysers to meet the 1.5°C climate goal, 2020, (Accessed 03 February 2025).
[49] PricewaterhouseCoopers (PwC), Green hydrogen cost: The key to the energy transition, 2025, (Accessed 03 February 2025).
[50] M. Münster, R. Bramstoft, I. Kountouris, L. Langer, D. Keles, R. Schlautmann, F. Mörs, C. Saccani, A. Guzzini, M. Pellegrini, A. Zauner, H. Böhm, D. Markova, S. You, M. Pumpa, F. Fischer, F. Sergi, G. Brunaccini, D. Aloisio, M. Ferraro, M. Mulder, H. Rasmusson, Perspectives on green hydrogen in europe—during an energy crisis and towards future climate neutrality, Oxf. Open Energy 3 (2024) oiae001.
[51] E. Panos, M. Densing, The future developments of the electricity prices in view of the implementation of the Paris agreements: Will the current trends prevail, or a reversal is ahead? Energy Econ. 84 (2019) 104476.
[52] Synergie Project, Electricity market design 2030 – 2050: Shaping future electricity markets for a climate neutral europe, 2021, (Accessed 03 February 2025).
[53] Eurelectric, Electrification action plan, 2025, (Accessed 03 February 2025).
[54] Bluefield Research, Europe's proactive policy approach advances US$476 billion water & wastewater capex outlook by 2030, 2024, (Accessed 03 February 2025).
[55] World Resources Institute, The world's highest water-stressed countries, 2024, (Accessed 03 February 2025).
[56] Water Europe, Water europe final report, 2024, (Accessed 03 February 2025).
[57] I. Dincer, M.A. Rosen, P. Ahmadi, Optimization of Energy Systems, John Wiley & Sons, 2017.
[58] M.S. Peters, K.D. Timmerhaus, R.E. West, Plant Design and Economics for Chemical Engineers, McGraw-Hill, 2003.
[59] R. Smith, Chemical Process Design and Integration, Wiley, 2005.
[60] Y. Du, L. Xie, J. Liu, Y. Wang, Y. Xu, S. Wang, Multi-objective optimization of reverse osmosis networks by lexicographic optimization and augmented epsilon constraint method, Desalination 333 (1) (2014) 66–81.
[61] M.D. Rosa, M. Carragher, D.P. Finn, Flexibility assessment of a combined heat-power system (CHP) with energy storage under real-time energy price market framework, Therm. Sci. Eng. Prog. 8 (2018) 426–438.
[62] O. Dumont, R. Dickes, M.D. Rosa, R. Douglas, V. Lemort, Technical and economic optimization of subcritical, wet expansion and transcritical organic rankine cycle (ORC) systems coupled with a biogas power plant, Energy Convers. Manage. 157 (2018) 294–306.
[63] V. Bianco, M.D. Rosa, F. Scarpa, L.A. Tagliafico, Implementation of a cogeneration plant for a food processing facility. a case study, Appl. Therm. Eng. 102 (2016) 500–512.
[64] T. Ioroi, K. Yasuda, Z. Siroma, N. Fujiwara, Y. Miyazaki, Thin film electrocatalyst layer for unitized regenerative polymer electrolyte fuel cells, J. Power Sources 112 (2) (2002) 583–587.
[65] G. Li, Organic rankine cycle environmental impact investigation under various working fluids and heat domains concerning refrigerant leakage rates, Int. J. Environ. Sci. Technol. 16 (1) (2019) 431–450.
[66] T. Li, Z. Zhang, J. Lu, J. Yang, Y. Hu, Two-stage evaporation strategy to improve system performance for organic rankine cycle, Appl. Energy 150 (2015) 323–334.
[67] V.E. Dudley, G.I. Kolb, A.R. Mahoney, T.R. Mancini, C.W. Matthews, M. Sloan, D. Kearney, Test Results SEGS LS-2 Solar Collector, Technical Report,, Sandia National Laboratories, Albuquerque, New Mexico, 1994, EChC Special Projects.